



**HAL**  
open science

## **40Ar/39Ar dating of high temperature geothermal systems: First attempt on hydrothermally altered pyroxenes from the Saintes archipelago (Lesser Antilles arc, Guadeloupe)**

Alexiane Favier, ChrysteLe Verati, Jean-Marc Lardeaux, Philippe Münch, Christophe Renac, Michel Corsini, François Orange

### ► To cite this version:

Alexiane Favier, ChrysteLe Verati, Jean-Marc Lardeaux, Philippe Münch, Christophe Renac, et al.. 40Ar/39Ar dating of high temperature geothermal systems: First attempt on hydrothermally altered pyroxenes from the Saintes archipelago (Lesser Antilles arc, Guadeloupe). *Chemical Geology*, 2021, 581, pp.120401. 10.1016/j.chemgeo.2021.120401 . hal-03280968

**HAL Id: hal-03280968**

**<https://hal.science/hal-03280968>**

Submitted on 2 Aug 2023

**HAL** is a multi-disciplinary open access archive for the deposit and dissemination of scientific research documents, whether they are published or not. The documents may come from teaching and research institutions in France or abroad, or from public or private research centers.

L'archive ouverte pluridisciplinaire **HAL**, est destinée au dépôt et à la diffusion de documents scientifiques de niveau recherche, publiés ou non, émanant des établissements d'enseignement et de recherche français ou étrangers, des laboratoires publics ou privés.



Distributed under a Creative Commons Attribution - NonCommercial 4.0 International License

# **$^{40}\text{Ar}/^{39}\text{Ar}$ dating of high temperature geothermal systems: first attempt on hydrothermally altered pyroxenes from the Saintes archipelago (Lesser Antilles arc, Guadeloupe)**

Alexiane Favier<sup>1-2-3\*a</sup>, Chrystele Verati<sup>2\*</sup>, Jean-Marc Lardeaux<sup>2-4</sup>, Philippe Münch<sup>5</sup>, Christophe Renac<sup>2</sup>, Michel Corsini<sup>2</sup> and François Orange<sup>6</sup>

1: UMR 5243 Géosciences Montpellier, Université des Antilles-CNRS-Université de Montpellier, Campus de Fouillole, 97159 Pointe-à-Pitre Cedex, Guadeloupe, France

2: UMR 7329 Geoazur, Université Côte d'Azur-CNRS-Observatoire de la Côte d'Azur, 250 rue Albert Einstein, Sophia-Antipolis, 06560 Valbonne, France

3 : Université de Lorraine-CNRS-GeoRessources, F-54000, France

4: Czech Geological Survey, Centre for Lithospheric Research, Klárov 3, 118 21 Prague 1, Czech Republic

5: UMR 5243 Géosciences Montpellier, Université de Montpellier-CNRS-Université des Antilles, Campus Triolet CC060, Place Eugène Bataillon, 34095 Montpellier, France

6: Université Côte d'Azur, Centre Commun de Microscopie Appliquée (CCMA), 06108 Nice, France

\* corresponding authors ([alexiane.favier@univ-lorraine.fr](mailto:alexiane.favier@univ-lorraine.fr), [chrystele.verati@univ-cotedazur.fr](mailto:chrystele.verati@univ-cotedazur.fr))

## **Abstract**

We investigate the potential of  $^{40}\text{Ar}/^{39}\text{Ar}$  systematics in secondary K-bearing minerals developed at the expense of hydrothermally altered volcanic pyroxenes from a fossil geothermal system located in the Saintes archipelago (Lesser Antilles magmatic arc).

Our work reports the first example of dating hydrothermal muscovite crystallization developed during pseudomorphic transformation of pyroxenes within altered rhyodacites at temperatures above 300°C. The white micas display a well-defined Ar/Ar plateau age of 2.59 ± 0.12 Ma, interpreted as the best age estimate for high temperature fluid circulation in the Saintes geothermal paleo-reservoir. A model of muscovite substitution by illite during cooling supports the interpretation that illitization perturbs the K-Ar and the Ar-Ar ages only when muscovite is highly illitized and/or if illitization is significantly younger than muscovite crystallization. The whole temporal dataset implies a fast cooling rate (>150°C/200 ka) and a maximal lifetime of 650 ka for the Saintes hydrothermal system.

**Keywords:**  $^{40}\text{Ar}/^{39}\text{Ar}$  dating, fossil geothermal system, hydrothermal reaction, meta-pyroxene, white mica, muscovite, illite

## **1. Introduction**

Tectonic settings favourable for high temperature geothermal energy are mainly located in areas with active volcanism, i.e., subduction, hotspot and rift zones (Arnórsson, 1995; Bibby *et al.*, 1995; Sasada *et al.*, 2000; Ragnarsson, 2015; Bertani, 2016; Barcelona *et al.*, 2019). Although many studies have explored structural, mineralogical, geochemical and geophysical characteristics to constrain the three-dimensional geometry of plumbing systems in active geothermal reservoirs, very few data are available on the duration of geothermal processes in active geothermal systems (Grimes *et al.*, 1998; Dalrymple *et al.*, 1999; Arehart *et al.*, 2002; Villa *et al.*, 2006; Wilson *et al.*, 2008; Verati *et al.*, 2014; Oze *et al.*, 2017). This lack of data is also true for epithermal systems that are recognized in magmatic arcs and commonly considered to be fossil geothermal systems (Brockamp *et al.*, 2003; Oliveros *et al.*, 2008; Hames *et al.*, 2009; Márton *et al.*, 2010). Indeed, very few minerals are available for geochronology within the hydrothermally altered domains recognized in geothermal fields

<sup>a</sup> Permanent address : [alexianefavier@outlook.com](mailto:alexianefavier@outlook.com)

52 worldwide. Usually, zircons from hydrothermally altered magmatic rocks are used with U-Pb  
53 and U-Th dating methods (Milicich et al., 2020; Rosenberg et al., 2020). Regarding the  
54  $^{40}\text{Ar}/^{39}\text{Ar}$  technique, most analyses attempted to date have been carried out on sericite,  
55 adularia, alunite, celadonite and clay minerals (Dong *et al.*, 1995; WoldeGabriel *et al.*, 1996;  
56 Hall *et al.*, 1997; Haines & van der Pluijm, 2008; Oliveros *et al.*, 2008; Clauer *et al.*, 2012;  
57 Clauer, 2013; Verati & Jourdan, 2014; Verati *et al.*, 2014; Oze *et al.*, 2017). These minerals  
58 suitable for the Ar-Ar method under epithermal conditions are mainly developed at the  
59 expense of primary magmatic feldspars. However, feldspars are often completely replaced  
60 by clay minerals during supergene alteration (Browne, 1978; Mas *et al.*, 2006). Thus, we  
61 need to find more dateable mineral systems for such geological conditions.

62 The aim of this article is to investigate the potential of  $^{40}\text{Ar}$ - $^{39}\text{Ar}$  systematics in secondary K-  
63 bearing minerals developed at the expense of volcanic pyroxenes in relation to high  
64 temperature hydrothermal fluid circulation within a fossil geothermal system located in the  
65 Lesser Antilles magmatic arc and more precisely in the Saintes archipelago.

66 This study focuses on the identification of K-bearing phases present in hydrothermally  
67 altered pyroxenes, hereafter called “meta-pyroxenes”, in order to decipher whether the Ar-Ar  
68 method can be appropriately applied in such a complex microstructure (i.e., pseudomorphic  
69 transformation) within which numerous secondary phases could be mixed. Dating the  
70 crystallization of minerals replacing volcanic pyroxenes offers a promising and new way to  
71 constrain the age and duration of hydro- or geo-thermal systems in subduction-related  
72 magmatic arcs.

## 73 74 **2. Geological setting and petrological framework**

75 In the active Lesser Antilles arc, the Saintes archipelago represents small volcanic islands  
76 (from the largest to the smallest islands: Terre-de-Bas, Terre-de-Haut, and their islets: Îlet à  
77 Cabris, Grand îlet and Îlet la Coche; Fig. 1-A and 1-B). These islands, in the framework of  
78 the Guadeloupe archipelago, are related to the recent active volcanic arc emplaced since  
79 4.28 Ma (Carlut et al., 2000; Samper et al., 2007; Samper et al., 2009; Ricci et al., 2015a;  
80 Ricci et al., 2015b; Ricci et al., 2017; Favier *et al.*, 2019). The Saintes Islands consist of  
81 typical calc-alkaline volcanic rocks, with ages ranging from  $2.00 \pm 0.03$  to  $2.98 \pm 0.04$  Ma for  
82 Terre-de-Haut Island and less than 1 Ma for Terre-de-Bas Island (Zami *et al.*, 2014).  
83 Volcanic formations include rhyodacite, dacite and andesite domes and/or lava flows  
84 associated with many debris flows and pyroclastic flows (Fig. 1-B).

85 In recent years, several studies (Verati et al., 2016; Navelot et al., 2018; Beauchamps et al.,  
86 2019; Favier et al., 2021) have identified this hydrothermal system as an eroded and  
87 exhumed geothermal system. In Terre-de-Haut Island, superposed fault networks are well  
88 known since pioneering investigations of Jacques and Maury (1988). In previous papers  
89 (Verati et al., 2016; Navelot et al., 2018) we demonstrated that the hydrothermal zone of  
90 Terre de Haut was located at a set of two intersecting fault families N090-N110 and N130-  
91 N140 delimiting it within a graben-like structure (Figure 1C) in relation to the overall tectonic  
92 setting of the volcanic arc (arc-perpendicular extension structures, Feuillet et al. 2002). We  
93 also discovered ductile tectonic structures, pressure solution cleavages, concentrated in  
94 schistose corridors intersected by the brittle faults (Figure 1 C, Favier et al., 2021). High-  
95 temperature hydrothermal phases crystallize in the schistose corridors (Favier et al., 2021)  
96 while low-temperature hydrothermal phases are mainly located in fractures, veins and brittle  
97 faults (Navelot et al., 2018; Beauchamps et al., 2019; Favier, 2019). At the scale of Terre-de-  
98 Haut Island, the finite strain pattern is heterogeneous and consequently the progressive high-  
99 temperature hydrothermal transformations of volcanic formations are identifiable from the  
100 undeformed, or slightly deformed area, to the most deformed shear zone.

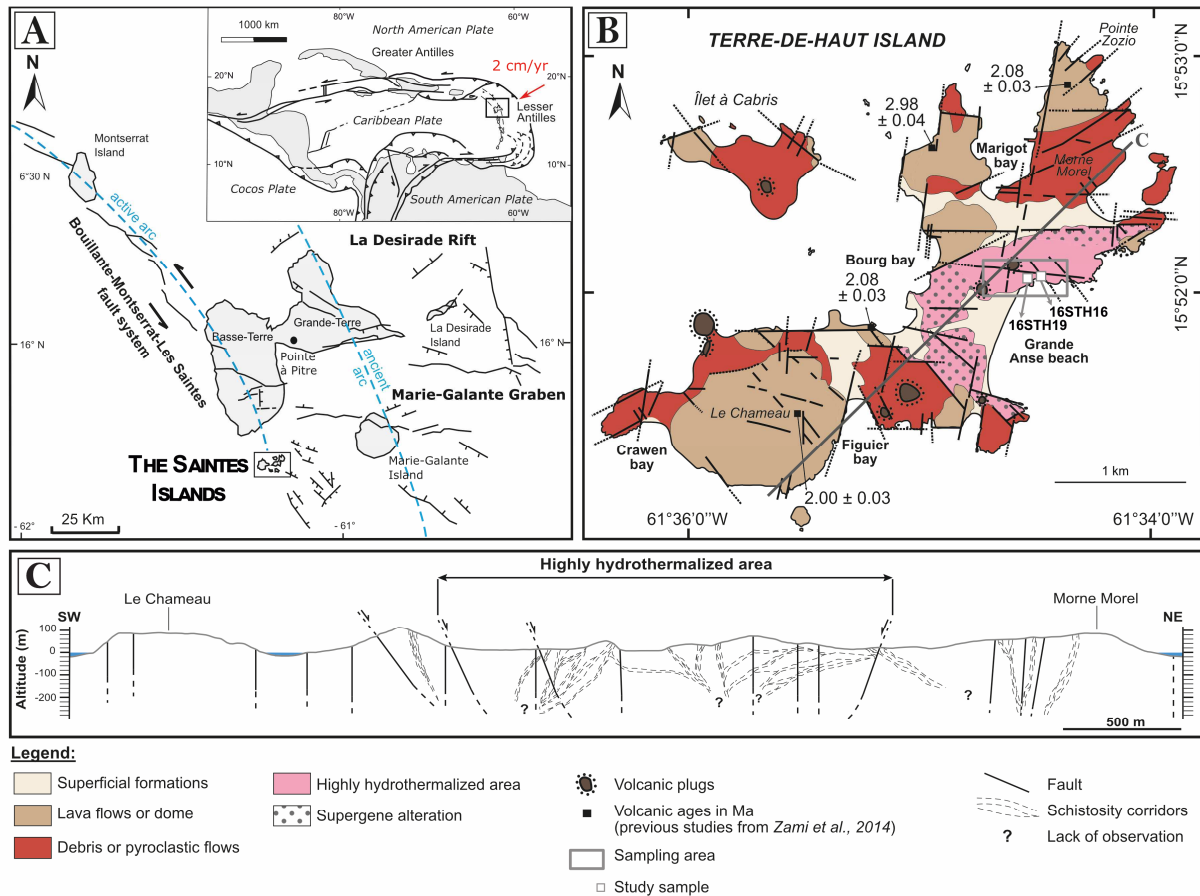


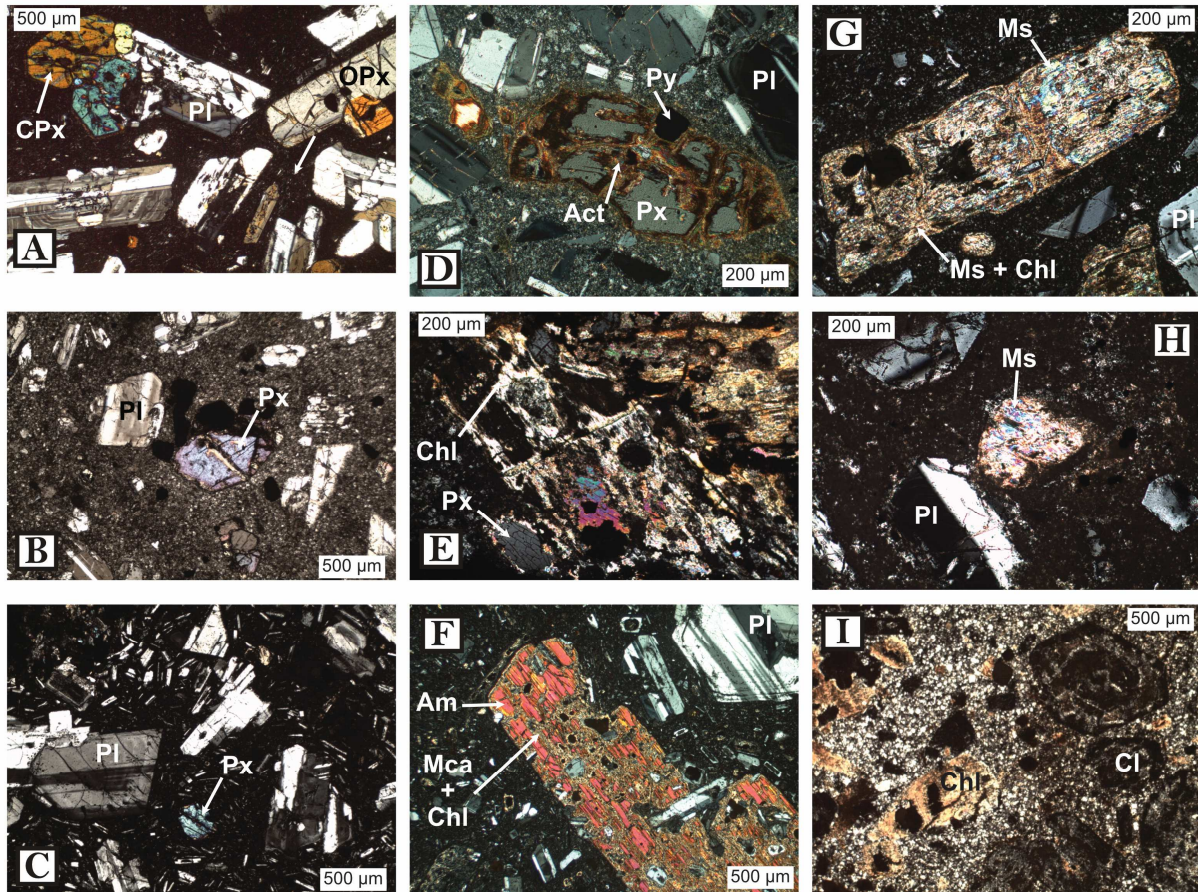
Figure 1: A) Location of the Lesser Antilles arc system and the Saintes archipelago (modified from Bouysse & Westercamp, 1990). The Saintes Islands are located in the inner active arc. B) Geological map of the Saintes archipelago (i.e., Terre-de-Haut and Îlet à Cabris; Terre-de-Bas is not shown). Volcanic K-Ar ages (Zami *et al.*, 2014) are reported. The location of the analysed samples are shown within the highly hydrothermalized area (after Verati *et al.*, 2016; Navelot *et al.*, 2018; Favier, 2019; Favier *et al.*, 2021). C) NE-SW cross-section (localization in fig.1-B) from Terre-de-Haut Island displaying the superposition of brittle faults upon the network of schistosity planes. The highly hydrothermalized area is located in the central part of the cross-section within a WNW-ESE graben (modify from Favier *et al.*, 2021).

### [Color]

Outside of the hydrothermal zone, fresh volcanic rocks display typical porphyritic textures (Fig. 2 A to C and 3-A and B). The chemistry and the number of phenocrysts are variable according to the lithotype of the volcanic rocks; in all samples, the following primary phases are always observed in decreasing order of abundance: plagioclases (mainly labradorites), clinopyroxenes (augites), orthopyroxenes (hypersthènes), amphiboles (hornblende to edenite or pargasite depending on the considered bulk-rock chemistry, Jacques & Maury, 1988) and Fe-Ti oxides (ilmenite or titanomagnetite). These volcanic rocks also show a volcanic groundmass rich in millimetre-sized microlites, mainly Fe-Ti oxides associated with anorthoclase in dacites and rhyodacites.

In the hydrothermal zone, the volcanic minerals (mainly pyroxene and amphibole) are partially or totally replaced by secondary phases (Fig. 2 D to H), and in the most altered rocks, the primary volcanic mineralogy has been totally erased (Fig. 2-I). However, where the rocks have escaped supergene alteration, the following secondary hydrothermal phases are observed at the rock sample scale (Favier *et al.*, 2021): albite + chlorite + muscovite + biotite + clinozoisite + epidote + titanite + quartz. This mineral association is typically described in active or fossil geothermal systems worldwide for temperatures ranging between 300 and 380°C (Browne, 1978; Henley & Ellis, 1983; Hedenquist & Browne, 1989; White &

131 Hedenquist, 1990; Groves *et al.*, 1998; Goldfarb *et al.*, 2001; Cherkose & Mizunaga, 2018).  
 132 The occurrence of secondary K-bearing minerals is particularly well developed in  
 133 hydrothermally altered pyroxenes (i.e., meta-pyroxenes), which suggests that  
 134 geochronological K-Ar and/or Ar-Ar methods can be applied here to date the hydrothermal  
 135 activity developed under these temperature conditions.  
 136

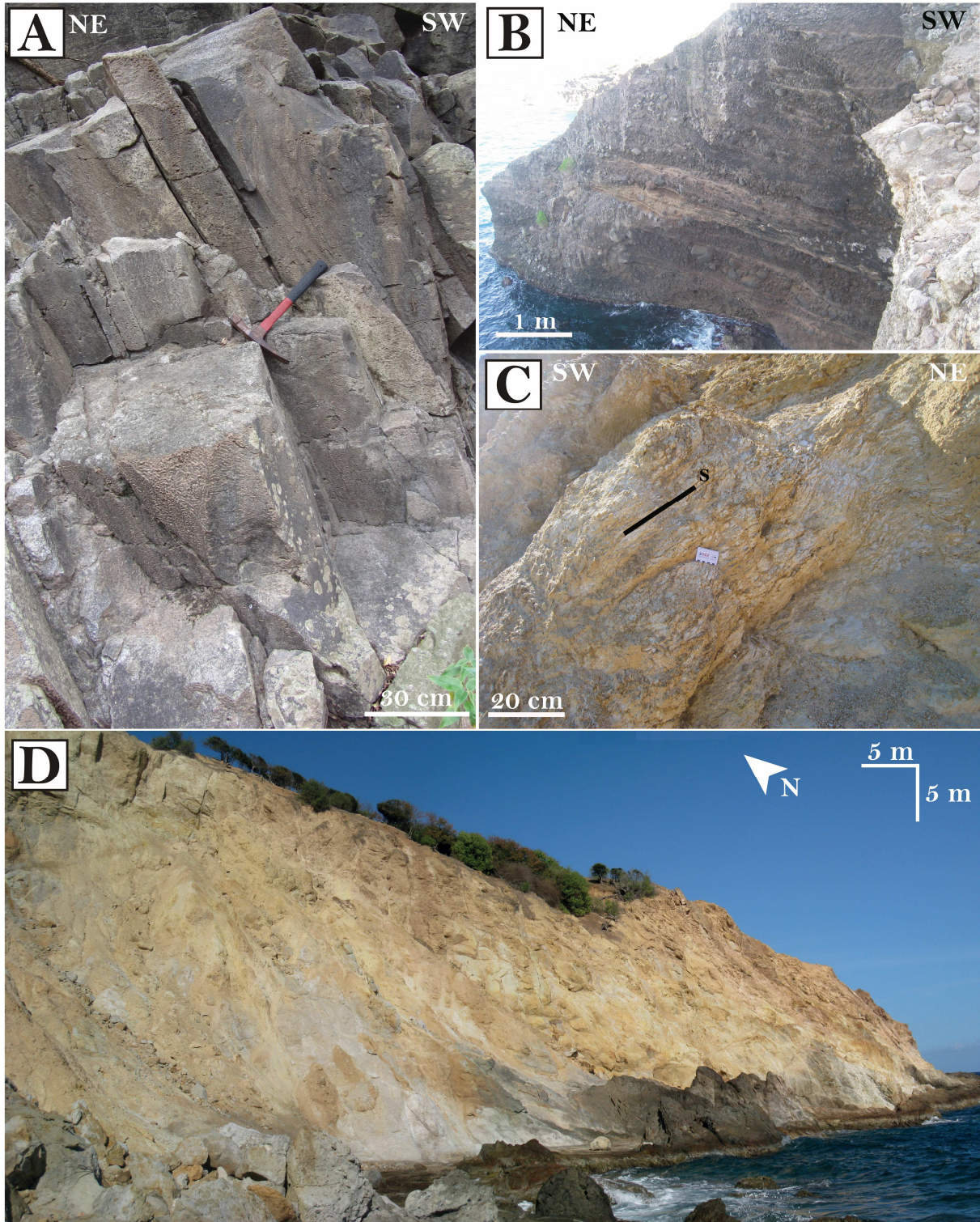


137  
 138 Figure 2: Some examples of volcanic textures found in Terre-de-Haut Island. A) Fresh  
 139 andesitic lava flow. B) Fresh dacitic lava flow. C) Andesite fragment from pyroclastic flow. D)  
 140 Altered andesitic lava flow, pyroxene partially replaced. E) Altered dacitic lava flow, volcanic  
 141 pyroxene partially replaced. F) Altered rhyodacite from a pyroclastic flow, volcanic  
 142 amphibole partially replaced. G) Volcanic pyroxene totally replaced by white mica and  
 143 chlorite, in an altered dacite of the highly hydrothermalized area. H) Volcanic pyroxene totally  
 144 replaced by white mica, in an altered dacite of the highly hydrothermalized area. I) Primary  
 145 volcanic mineralogy totally erased (plagioclase and pyroxene replaced respectively by clays  
 146 minerals and chlorite), in a highly altered rhyodacite. Act = actinolite, Am = amphibole, Chl =  
 147 chlorite, Cl = clay minerals, Mca = mica, Ms = muscovite, PI = plagioclase, Px = pyroxene (C  
 148 = clino- and O = ortho-), Py = pyrite.

### 149 3. Materials and Methods

150  
 151 After recovering 35 samples in the field from the highly hydrothermalized area of Terre-de-  
 152 Haut Island (Fig. 1-B, 3-C and D) and based on subsequent preliminary observations of thin  
 153 sections, we selected two samples (16STH16 and 16STH19) that are not affected by  
 154 supergene alteration and contain meta-pyroxene crystals developed well enough to perform  
 155 mineralogical measurements. To carry out further geochronological investigations, we chose  
 156 sample 16STH19, in which the meta-pyroxenes were the most highly developed. After  
 157 crushing this rock, we selected the 315-500  $\mu\text{m}$  size fraction representing the apparent meta-  
 158 pyroxene size distribution in thin section. A series of magnetic separations (Frantz  
 159 Isodynamic® Separator Model L-1) applied to grains allowed the removal of sulphide and

160 oxide crystals and the concentration of meta-pyroxenes in the less magnetic aliquot. After  
161 HNO<sub>3</sub> leaching (1 N, 70°C) for a few hours to avoid residual oxide or sulphide inclusions, this  
162 fraction was repeatedly cleaned with an ultrasonic bath in distilled water, rinsed with ethanol  
163 and dried (<50°C). The remaining grains were handpicked under a binocular microscope  
164 (Fig. 4). We performed scanning electron microscopy and electron microprobe  
165 measurements on thin sections and X-ray diffraction from this separated 315-500 μm fraction  
166 to characterize the morphology, mineralogy and chemistry of these meta-pyroxene grains.  
167



168 Figure 3: A) Fresh andesitic lava flow from Le Chameau. B) Fresh pyroclastic flow from  
169 Pointe Zozio. C) Sampling area (north of Grande Anse beach) in the highly hydrothermalized  
170

171 area where primary volcanic formations are severely reworked and affected by a schistosity  
172 plane (s). D) Sampling area (north of Grande Anse beach) showing intense rock  
173 transformations. **[Color for online version only]**  
174



175  
176 Figure 4: Selected meta-pyroxene grains (315-500  $\mu\text{m}$  fraction) after magnetic separation,  
177  $\text{HNO}_3$  leaching and handpicking. **[Color for online version only]**  
178

### 179 3.1. Electron microprobe analysis

180 Electron probe microchemical analysis (EPMA), using a CAMECA SX-100 electron  
181 microprobe at the “Service Commun de Microsonde” of Montpellier University, was  
182 performed on the sample 16STH16 and 16STH19 thin sections to precisely identify the  
183 different minerals within the meta-pyroxenes. The operating conditions were a 20 kV  
184 accelerating voltage and 10 nA beam current.  
185

### 186 3.2. Scanning electron microscopy

187 Scanning electron microscopy (SEM) and energy-dispersive X-ray spectroscopy (EDX) were  
188 performed at the “Centre Commun de Microscopie Appliquée” of the Université Côte d’Azur  
189 on the sample 16STH16 and 16STH19 thin sections and polished surfaces using a Tescan  
190 Vega 3 XMU SEM system (TESCAN FRANCE, Fuveau, France) equipped with an X-MaxN  
191 50 EDX detector (Oxford Instruments, Abingdon, U.K.) to identify the chemical element  
192 distributions and compositions within the meta-pyroxenes. Thin sections were carbon coated,  
193 while no coating was used for polished surfaces. Samples were observed and analysed  
194 using the low vacuum mode of the SEM ( $\text{N}_2$  pressure: 10 Pa for thin sections and 25 Pa for  
195 polished surfaces) at an accelerating voltage of 20 kV. EDX results were processed with the  
196 Aztec software (version 3.1, Oxford Instruments).  
197

### 198 3.3. X-ray diffraction method

#### 199 3.3.1. Sample preparation

200 An aliquot of the whitish grains (315-500  $\mu\text{m}$  fraction) was crushed to a fine powder (<70  $\mu\text{m}$ )  
201 and was analysed by X-ray diffraction (XRD, Panalytical X’pert Pro system, Bragg Brentano  
202 geometry, PIXcel detector  $\text{CuK}_{\alpha 1+2}$ , counting step  $0.07^\circ 2\theta$ , angles from  $3.5$  to  $75^\circ 2\theta$ ) at the

203 CEMEF laboratory (Ecole des Mines in Sophia-Antipolis Scientific Centre, France). Mineral  
204 identification was established using the Match! software (v. 3.9.0.158, “COD-20190910”  
205 database).

206 Second, in order to characterize microcrystalline phyllosilicates identified in thin sections, we  
207 soaked the whitish grains in a CaCl<sub>2</sub> solution (250 g.L<sup>-1</sup>) for 4 days to saturate the interlayer  
208 spacing of clay minerals with Ca. Later, the mixture of grains and CaCl<sub>2</sub> was rinsed with  
209 demineralized water up to an electrical conductivity of 40 μS.cm<sup>-1</sup> and centrifuged to recover  
210 the dispersed particles in water. The fine particles (<2 μm) were collected for phyllosilicate  
211 identification and deposited on a silica glass wafer. XRD analyses were performed on these  
212 <2 μm samples (parameters identical to the <70 μm fraction according to angles from 2 to  
213 35° 2θ) at the same CEMEF laboratory. The <2 μm phyllosilicate fractions were analysed  
214 under air-drying (AD) with 45% relative humidity and with liquid ethylene glycol (EG) to  
215 identify smectites from other minerals (chlorite or illite).

### 216 3.3.2. Decomposition of XRD patterns for <2 μm samples

217 A preliminary decomposition of peaks in AD and EG XRD patterns was performed using the  
218 Fityk 1.5 peak fitting software (Wojdyr, 2010). The different XRD patterns (AD and EG) were  
219 decomposed on bands of illite (001), mica (001), chlorite (002), and EG-smectite (001),  
220 according to Lanson (1997). The full width at half maximum (FWHM) is used to describe the  
221 crystallinity or crystal ordering of phyllosilicates with the Kubler (micaceous phases, see  
222 below, Kübler, 1967) and Arkai (chlorite, Arkai, 1991) indexes. Furthermore, in the remainder  
223 of this text, the 10 Å (001) peak with a FWHM lower than 0.17 is described as muscovite,  
224 between 0.17 and 0.27 as illite-muscovite, between 0.27 and 0.53 as illite and higher than  
225 0.53 as illite-smectite (Warr & Cox, 2016). The relative proportions of phyllosilicates were  
226 estimated on both the surface and FWHM of decomposed peaks in EG patterns for (001).  
227 XRD patterns (AD and EG) of <2 μm samples extracted from the 315-500 μm size fractions  
228 were deconvoluted with the PyXRD Linux software developed by Dumon and van Ranst  
229 (2016). This program compares oriented patterns (AD and EG) and calculated XRD profiles.  
230 The calculated XRD allows calculation of the proportion and stacking sequences of  
231 muscovite/illite, chlorite, smectite and interlayered illite/smectite.

232

### 233 3.4. Ar-Ar dating

234 Approximately 500 white grains of meta-pyroxene (Fig. 4) from sample 16STH19 were  
235 handpicked under a binocular microscope. Selected grains were packed in aluminium foils  
236 for irradiation in the core of the Triga Mark II nuclear reactor at Pavia (Italy) with several  
237 aliquots of sanidine from the Taylor Creek Rhyolite standard (28.619 ± 0.034 Ma; Renne *et*  
238 *al.*, 2010) as the flux monitor. Argon isotope interferences on K and Ca were determined by  
239 irradiation of KF and CaF<sub>2</sub> pure salts from which the following correction factors were  
240 obtained: (<sup>40</sup>Ar/<sup>39</sup>Ar)<sub>K</sub> = 9.69 × 10<sup>-3</sup> ± 3.6 × 10<sup>-5</sup> at 1σ, (<sup>38</sup>Ar/<sup>39</sup>Ar)<sub>K</sub> = 1.297 × 10<sup>-2</sup> ± 4.5 × 10<sup>-4</sup> at  
241 1σ, (<sup>39</sup>Ar/<sup>37</sup>Ar)<sub>Ca</sub> = 7.27 × 10<sup>-4</sup> ± 4.0 × 10<sup>-5</sup> at 1σ, and (<sup>36</sup>Ar/<sup>37</sup>Ar)<sub>Ca</sub> = 2.88 × 10<sup>-4</sup> ± 1.6 × 10<sup>-5</sup> at  
242 1σ. The <sup>40</sup>Ar/<sup>39</sup>Ar step heating analyses were performed at Geosciences Montpellier  
243 (France). After irradiation, four aliquots of bulk sample were analysed (between 100 and 150  
244 grains per analysis). The gas extraction and purification line consisted of (a) an IR-CO<sub>2</sub> 100  
245 kHz laser used at 3–20% power to heat samples for 180 s, (b) a lens system for beam  
246 focusing, (c) a steel chamber, maintained at 10<sup>-8</sup>–10<sup>-9</sup> bar, with a copper holder in which 2  
247 mm-diameter blind holes were milled, and (d) two ZrAl getters for purification of gases. Argon  
248 isotopes were measured in static mode using an ARGUS VI mass spectrometer.  
249 Measurements were carried out in multi-collection mode using Faraday cups. Analyses of  
250 atmospheric argon and <sup>36</sup>Ar, <sup>38</sup>Ar and <sup>40</sup>Ar isotopes (‘air pipette’) were regularly obtained for  
251 mass discrimination estimates. The raw data from each step and blanks were processed,  
252 and ages were calculated using the ArArCALC software (ArArCalc version 2.52; Koppers,  
253 2002). Blanks were monitored after every three step heating analyses. All parameters and  
254 relative abundance values for each experiment are provided in the supplementary data  
255 (Ar/Ar experiments file). The calculated proportions of Ar isotopes were corrected for blanks,  
256 mass discrimination, and radioactive decay. Atmospheric <sup>40</sup>Ar was estimated using a value of  
257 the initial <sup>40</sup>Ar/<sup>36</sup>Ar of 298.56 (Lee *et al.*, 2006). Our criteria for the determination of a plateau

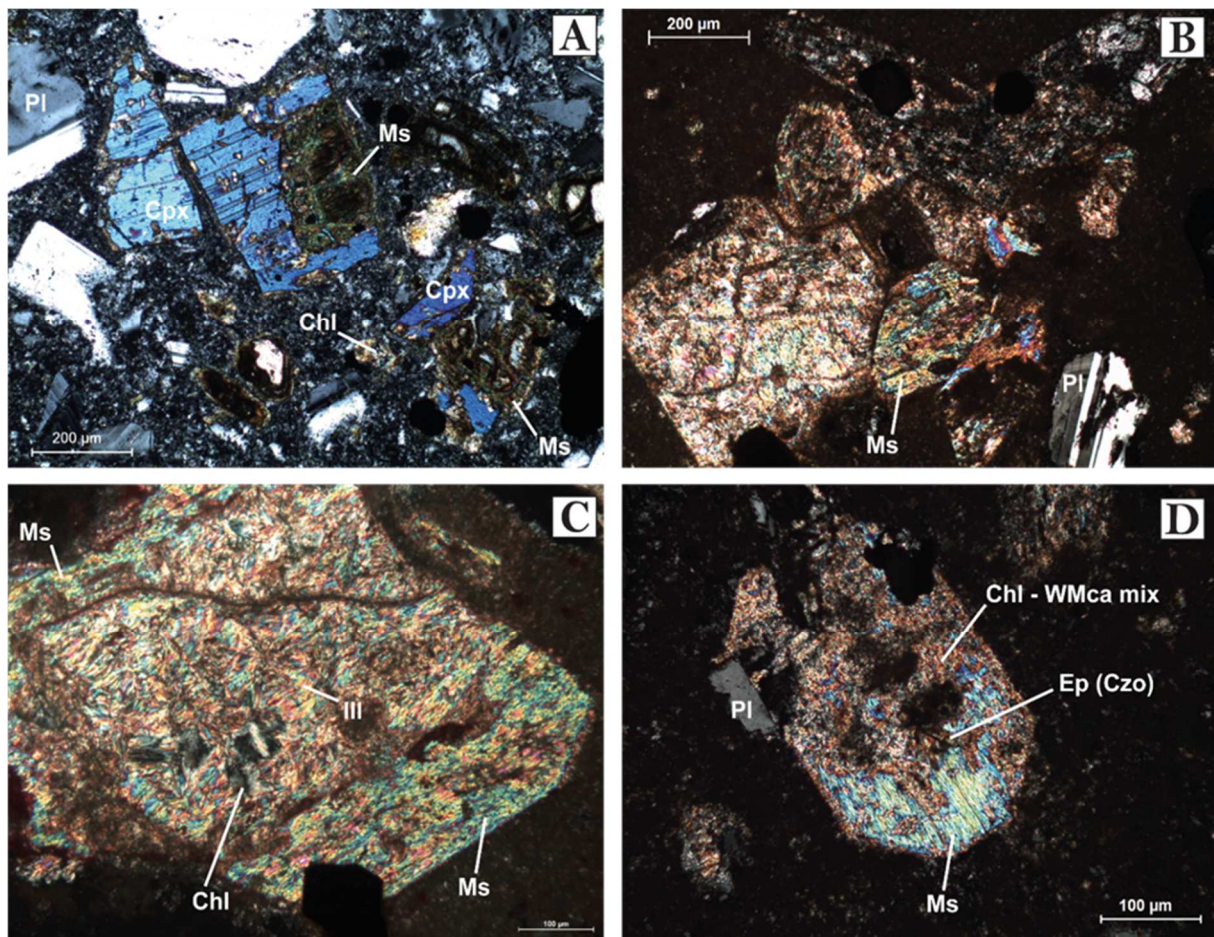


258 were as follows: a plateau must include at least 60% of released  $^{39}\text{Ar}$  over a minimum of  
259 three consecutive steps agreeing at the 95% confidence level. Plateau ages are given at the  
260  $2\sigma$  error level, and the plateau age uncertainties include analytical and J-value errors.  
261 Because through the history of a given geothermal system, several quick spurs of heat from  
262 deep below are still possible, the interpretation of age and duration of the studied system will  
263 be discussed according to its possible mineralogical evolutions.

#### 264 4. Results

##### 265 4.1. Pseudomorphic transformation of volcanic pyroxenes

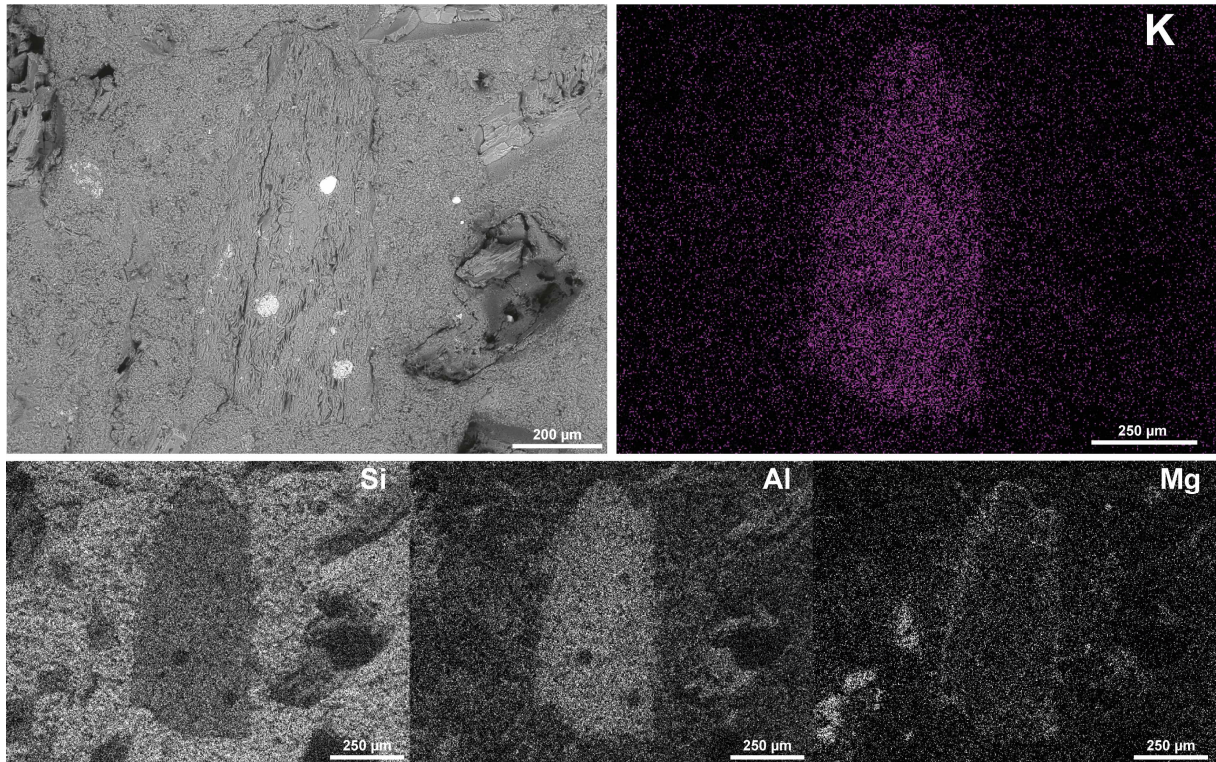
266 When comparing all volcanic rocks in the study area, the most spectacular pseudomorphic  
267 transformations of pyroxenes are found in hydrothermalized dacites and rhyodacites. Indeed,  
268 in the thin sections of these samples, we observe various degrees of pseudomorphic  
269 transformation of volcanic pyroxenes in relation to kinetics and thus progress of hydrothermal  
270 reactions. In some cases, pyroxenes are only partly replaced by flaky white micas  
271 (muscovite, Fig. 5-A). On the other hand, we also observe fully transformed pyroxenes (Fig.  
272 5-B). When the reaction is complete, small patches of flaky particles suggest the occurrence  
273 of chlorite and illite or mixed-layered illite/smectite (I-S) minerals (Fig. 5-C). Texturally, fibrous  
274 illites or I-S (sheaf felting) are developed at the expense of muscovite. Consequently, in  
275 some cases, the product of the fully achieved pseudomorphic pyroxene transformation is a  
276 microcrystalline mixture of muscovite+illite (or I-S)+chlorite. In a restricted number of cases,  
277 epidote (Fig. 5-D) and titanite are also recognized in flaky particles or thin patches  
278 surrounding the pseudomorphosed pyroxenes.  
279



280 Figure 5: Photomicrographs showing pseudomorphic transformations of pyroxenes A) Thin  
281 section of hydrothermalized dacite sample (sample from southwest of Bourg Bay)  
282 with partially transformed pyroxene; B) Fully transformed pyroxene in hydrothermalized  
283 rhyodacite sample (sample from north of Grande Anse beach, 16STH19); C) Meta-pyroxene  
284 with muscovite and chlorite (sample from north of Grande Anse beach, 16STH19); and D)  
285

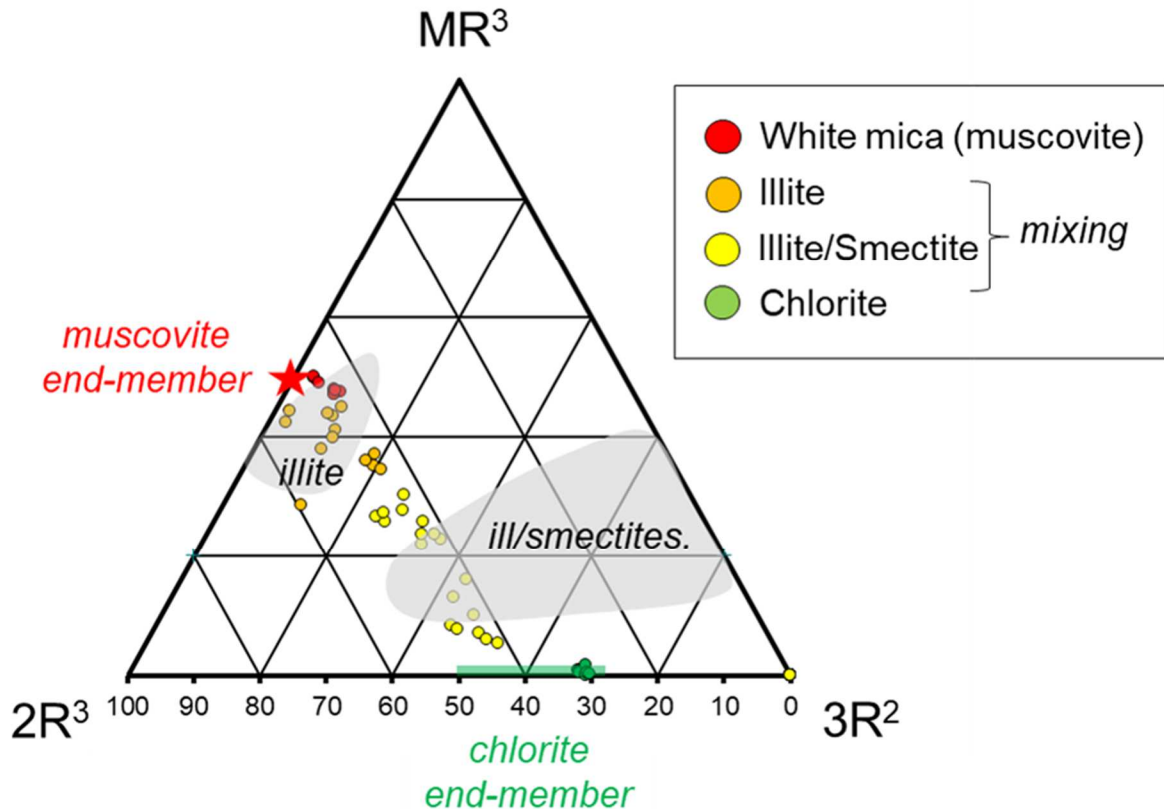
286 Meta-pyroxene with fibrous aggregates of chlorite and white micas developed at the expense  
287 of muscovite in hydrothermalized dacite sample (sample from north of Grande Anse beach,  
288 16STH16). Chl = chlorite, Cpx = clinopyroxene, Czo = clinozoisite, Ep = epidote, Ill = illite, Ms  
289 = muscovite, Pl = plagioclase, Wmca = white mica **[Color]**

290  
291 EDX spot analysis and chemical mapping made with SEM on several meta-pyroxenes in thin  
292 sections (Fig. 6) and isolated grains allow us to determine their elementary chemical  
293 compositions and the average K content (with an average of 5 wt %). Thus, we can identify  
294 the K-bearing phases within a wide range of white micas (muscovite +/- illite or I-S) in these  
295 grains.  
296



297  
298 Figure 6: BSE image and chemical compositional maps (K, Si, Al and Mg elements) of  
299 muscovite in a meta-pyroxene grain obtained by EDX analyses. **[Color]**

300  
301 The large flakes of muscovite, chlorite and the smaller microcrystalline aggregates were  
302 analysed with EPMA for major element composition (online supplementary data, Table A.1).  
303 The structural formulae of minerals were calculated relative to a structure containing 11  
304 oxygen atoms (muscovite, illite, I-S) or 14 oxygen atoms (chlorite), assuming that the total  
305 iron content was composed of Fe<sup>3+</sup>. In the MR<sup>3</sup>-2R<sup>3</sup>-3R<sup>2</sup> diagram (Fig. 7), chlorite and white  
306 mica compositions are close to the pure chlorite (sudoite to donbassite types, Wiewióra &  
307 Weiss, 1990) and muscovite end-members, respectively, while the microcrystalline mixtures  
308 ranging between muscovite and chlorite compositions are compatible with illite and I-S  
309 domains (Fig. 7).  
310

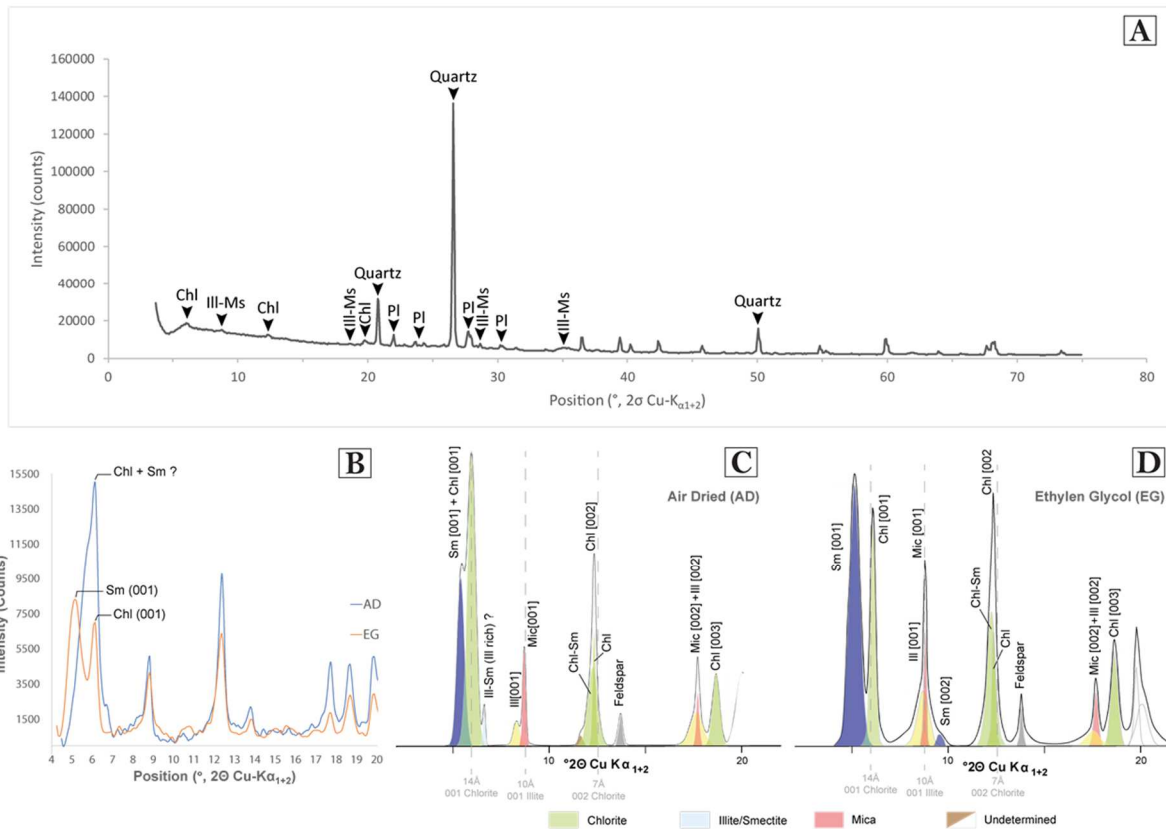


311  
 312 Figure 7: Chemical compositions of secondary phases in the  $MR^3$ - $2R^3$ - $3R^2$  diagram (Velde,  
 313 **1985**). Well-distinguished muscovite and chlorite patches, observed in thin sections, are  
 314 nearly pure end-members. Analyses of undefined microcrystalline aggregates indicate  
 315 heterogeneous compositions between the illite and illite/smectite fields. Data are available in  
 316 the online supplementary data (EPMA data – Table A.1). **[Color]**

317  
 318 **4.2. Crystallography and mineralogy of secondary minerals in**  
 319 **pseudomorphosed pyroxenes**

320 X-ray diffraction analyses of the separated 315-500  $\mu\text{m}$  fraction hosting the meta-pyroxene  
 321 grains yield quartz, feldspar, illite-muscovite and chlorite, with no XRD peak for pyroxene  
 322 (Fig. 8-A). The FWHM of the quartz and feldspar (labradorite) vary from 0.12 to 0.18°  $2\theta$ ,  
 323 suggesting that these phases are well crystallized and correspond to volcanic phases. The  
 324 muscovite-illite and chlorite peaks are expressed at low angles (2 to 20°) and correspond to  
 325 secondary minerals replacing the primary pyroxenes. The FWHM of (001) mica and chlorite  
 326 measured on the bulk grain mineralogy with several minerals and the separation of clay-size  
 327 particles with insufficient material do not allow the identification of mica polytypes (1M, 2M,  
 328 including 2M1 and 2M2, or 3T type).

329 To better characterize these mica polytypes, we separated the <2  $\mu\text{m}$  fine particles from the  
 330 bulk fraction. In this finest fraction, the X-ray patterns (oriented AD and EG, Fig. 8-B) allow us  
 331 to identify less abundant and small particles roughly recognized in thin sections (Fig. 5-C),  
 332 i.e., chlorite, smectite, mica, mica-illite and I-S species. The identified relative assemblages  
 333 for the meta-pyroxenes are reported in Table 1. In order of decreasing abundance (Tab. 1  
 334 and online supplementary data in Tab. A.2), we record (Fig. 8-C): (1) pure illite/muscovite  
 335 with well-crystallized muscovite (small Kübler indexes of 0.12 for (001) mica and 0.53 for  
 336 (001) illite), (2) pure smectite, (3) interstratified chlorite-smectite (Fig. 8-D), and (4) pure  
 337 chlorite (with an Arkai index of 0.34). Even in the finest fraction residues of volcanic  
 338 labradorite can still be observed.  
 339



340  
 341 Figure 8: A) XRD bulk meta-pyroxene sample (16STH19); B) Raw X-ray diffraction patterns  
 342 in AD (air dried) and EG (ethylene glycol) states; C) Decomposed and modelled X-ray  
 343 patterns in the AD state; D) Decomposed and modelled X-ray patterns in the EG state.  
 344 **[Color for online version only]**  
 345

346 Table 1: Results of <2 μm mineral assemblages from the meta-pyroxene using the AD state.  
 347 The Årkai and Kübler indexes are also reported for detected chlorite, illite and white mica.  
 348 Estimates of related T<sub>min</sub> values for illite and white mica are determined after Warr and Cox,  
 349 2016. Chl = chlorite, Fsp = feldspar, Ill = illite, I-S = interlayered illite-smectite, Musc =  
 350 muscovite, Sm = smectite. **[Color for online version only]**

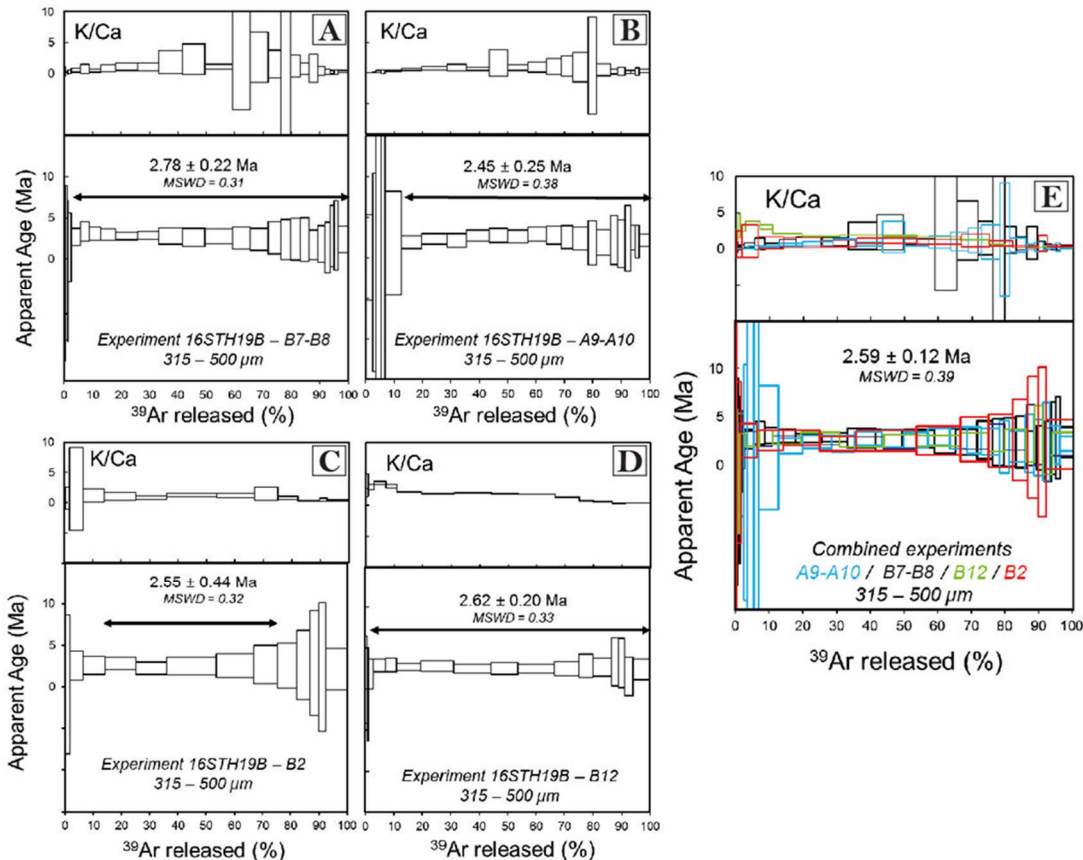
Årkai index	Kübler index		T <sub>min</sub> values [001 illite]	T <sub>min</sub> values [001 mica]	<2μm assemblage
002 chlorite	001 illite	001 mica	(Warr and Cox, 2016)	(Warr and Cox, 2016)	
0.34	0.53	0.12	>200°C	>350°C	Ill-Musc, Sm, Chl-Sm, Chl, Fsp

351  
 352 The K-rich phases, which can play a role in the obtained <sup>40</sup>Ar/<sup>39</sup>Ar dataset, are well identified  
 353 in our sample: muscovite, illite and interstratified I-S. Other phases without potassium  
 354 (chlorite, smectite, quartz, labradorite, epidote, titanite or absent pyroxene) can be neglected  
 355 compared to K-bearing phases.  
 356

### 357 4.3. Ar-Ar results

358 All detailed data for each experiment are provided in the online supplementary data (Ar/Ar  
 359 experiments file) with a compilation of Ar-Ar results available in Table A.3.  
 360 As previously mentioned, four aliquots of the same sample (16STH19B) were replicated. The  
 361 first experiment (16STH19B B7-B8) yields a well-defined plateau age of 2.78 ± 0.23 Ma,  
 362 corresponding to 97.6% of <sup>39</sup>Ar released (Fig. 9-A). The inverse isochron calculation yields  
 363 an identical age of 2.77 ± 0.33 Ma with an initial <sup>40</sup>Ar/<sup>36</sup>Ar ratio of 299.9 ± 12.6, indicating that  
 364 the trapped <sup>40</sup>Ar/<sup>36</sup>Ar is indistinguishable from atmospheric <sup>40</sup>Ar/<sup>36</sup>Ar. The second and third  
 365 experiments (16STH19 A9-A10 and 16STH19 B12) display concordant plateau ages at 2.45  
 366 ± 0.25 Ma and 2.62 ± 0.20 Ma, with 87.3% and 98.9% of <sup>39</sup>Ar released, respectively (Fig. 9-  
 367

368 B-D). Inverse isochron ages and related initial  $^{40}\text{Ar}/^{36}\text{Ar}$  ratios for these two experiments are  
 369 concordant with those for the first aliquot. The fourth experiment, 16STH19B B2, yields a  
 370 less well-defined plateau age of  $2.55 \pm 0.44$  Ma (Fig. 9-C), with 61% of  $^{39}\text{Ar}$  released due to  
 371 higher  $^{40}\text{Ar}$  atmospheric contamination. Nevertheless, all plateau ages are concordant; thus,  
 372 we can statistically combine these four experiments. We retain the combined plateau age at  
 373  $2.59 \pm 0.12$  Ma at  $2\sigma$  (MSWD 0.39) for meta-pyroxenes (Fig. 9-E). K/Ca spectra (deduced  
 374 from  $^{39}\text{Ar}_K/^{37}\text{Ar}_{Ca}$  spectra) associated with the four plateau ages display relatively regular flat  
 375 patterns, highlighting the chemical reproducibility of the step-heated phase(s).  
 376



377  
 378 Figure 9:  $^{40}\text{Ar}/^{39}\text{Ar}$  age spectra and K/Ca spectra as functions of  $^{39}\text{Ar}$  released. The error  
 379 boxes of each step are at the  $2\sigma$  level. Arrows show the plateau age fraction. The error of the  
 380 plateau age is given at the  $2\sigma$  level. A, B, C and D: Four individual experiments on the meta-  
 381 pyroxene 315-500  $\mu\text{m}$  fraction; E: Combined spectra of the four experiments A+B+C+D.  
 382 [Color]

## 384 5. Discussion

385 Based on previously described petrographic and mineralogical observations, the evolution  
 386 observed in meta-dacites or meta-rhyodacites resulted mainly in the development of white  
 387 micas and chlorite at the expense of pyroxenes during the high temperature stage.  
 388 Microcrystalline clay mineral assemblages developed afterward during the low-temperature  
 389 stage of the hydrothermal system. This process requires (1) significant  $\text{H}_2\text{O}$ -rich fluid  
 390 infiltration through the pore space of the rocks and the volcanic groundmass with partial  
 391 dissolution of at least anorthoclase microlites, which are the only possible local source of K,  
 392 and (2) transfer of K, Si, and Al in the fluid-free phase until contact with pyroxene  
 393 phenocrysts.

### 395 5.1. Influence of K-rich phase crystallinity on Ar-Ar result interpretations

396 Interstratified I-S species with low crystallinity are frequently developed at the expense of  
 397 muscovite in numerous hydrothermal systems (Inoue *et al.*, 1992; Inoue & Kitagawa, 1994).

398 This mineralogical transformation would perturb the previous K-bearing phase chronometer  
 399 and thus would provide complex and disturbed Ar-Ar spectra. Nevertheless, we obtain well-  
 400 defined Ar-Ar plateau ages from the analysed meta-pyroxene grains, which is most likely due  
 401 to the abundance of muscovite with high crystallinity in the pseudomorphic assemblage.  
 402 However, the analysed grains are a mixture of mainly muscovite and various proportions of  
 403 clay minerals, including K-rich phases, i.e., illite and I-S that crystallized at different  
 404 temperatures and thus at different times. The flat K/Ca spectrum that we obtained in all  
 405 replicates does not resemble that of biphasic assemblages. This result suggests that cooling  
 406 was fast enough to preserve muscovite from low-temperature transformations. Because of  
 407 the presence of illite, we could not exclude a possible  $^{39}\text{Ar}$  recoil effect and thus disturbed  
 408 ages, as previously described by various authors (Dong *et al.*, 1995; Hall *et al.*, 1997; Isik *et*  
 409 *al.*, 2014). Indeed, the recoil effect, occurring during neutron irradiation, affects < 50  $\mu\text{m}$   
 410 microcrystals (Jourdan *et al.*, 2007) and here specifically the illite species. However, the  
 411 reproducibility of our four individual experiments (Fig. 9), without typical recoil spectra,  
 412 enhances the reliability of the Ar-Ar plateau age obtained.  
 413

## 414 5.2. Influence of hydrothermal system cooling on Ar-Ar results

415 In thin sections, we observe the development of illite at the expense of well-crystallized  
 416 muscovite grains (Fig. 5-C). This observation is consistent with other studies indicating that  
 417 under low-grade metamorphism as well as under hydrothermal alteration conditions, the  
 418 secondary micas developed at the expense of pyroxenes are often mixed illite and muscovite  
 419 (Meyer & Hemley, 1967; Merriman & Peacor, 1998). Moreover, several studies have  
 420 demonstrated that muscovite develops in epithermal to mesothermal systems at  
 421 temperatures above 300°C (Guilbert & Park, 1986; White & Hedenquist, 1990; Groves *et al.*,  
 422 1998; Hedenquist *et al.*, 2000; Goldfarb *et al.*, 2001), while illite is stable at lower  
 423 temperatures, and its crystallization is generally the result of cooling of the hydrothermal  
 424 system (~150°C, Henley & Ellis, 1983; Hedenquist *et al.*, 2000; Ji & Browne, 2000; Warr &  
 425 Cox, 2016). It therefore seems important to test the effect of illite development during cooling  
 426 of the studied samples on our Ar-Ar results.

427 To quantify the effect of illite development on the muscovite age, we propose a theoretical  
 428 model showing how progressive illite formation modifies the K-Ar systematics of muscovite  
 429 and ultimately can affect the accuracy of muscovite ages.

430 The calculations proposed for sericitization of plagioclases by Verati and Jourdan (2014) are  
 431 hereafter similarly applied to muscovite and illite in pseudomorphosed pyroxenes. This  
 432 calculation evaluates the K-Ar age reductions of illitized muscovite with a two-component  
 433 mixture between hydrothermal primary muscovite and secondary illite, considering that  
 434 illitization occurs in a single stage.

435 Using the K-Ar age equation, for a given K content in muscovite ( $^{40}\text{K}_{ms}$ ), the radiogenic  $^{40}\text{Ar}$  in  
 436 illite-free muscovite with an age  $t$  is:

$$437 \quad {}^{40}\text{Ar} = \frac{\lambda_e}{\lambda} {}^{40}\text{K}_{ms} (e^{\lambda t} - 1)$$

438 For muscovite that is illitized at  $t'$  ( $t' < t$ ), with  $X\%$  illite in the mixture, for a given K content in  
 439 illite ( $^{40}\text{K}_{ill}$ ), the total amount of K content in the mixture ( $^{40}\text{K}_{tot}$ ), as well as the total amount of  
 440 radiogenic  $^{40}\text{Ar}$  ( $^{40}\text{Ar}_{tot}$ ) in the mixture, are:

$$441 \quad {}^{40}\text{K}_{tot} = (1 - X) {}^{40}\text{K}_{ms} + X {}^{40}\text{K}_{ill} \quad \text{with} \quad {}^{40}\text{Ar}_{tot} = {}^{40}\text{Ar}_{ms} + {}^{40}\text{Ar}_{ill}$$

442 We obtain:

$$443 \quad {}^{40}\text{Ar}_{tot} = \frac{\lambda_e}{\lambda} {}^{40}\text{K}_{ms} (e^{\lambda t} - 1) + \frac{\lambda_e}{\lambda} {}^{40}\text{K}_{ill} (e^{\lambda t'} - 1)$$

444 We can define the apparent age  $t''$  of the two-component mixture (illitized muscovite) as  
 445 follows:

$$446 \quad {}^{40}\text{Ar}_{tot} = \frac{\lambda_e}{\lambda} {}^{40}\text{K}_{tot} (e^{\lambda t''} - 1)$$

447  
 448 The previous equations may be combined to give:

449 
$$\frac{\lambda_e}{\lambda} {}^{40}K_{tot}(e^{\lambda t''} - 1) = \frac{\lambda_e}{\lambda} {}^{40}K_{ms}(e^{\lambda t} - 1) + \frac{\lambda_e}{\lambda} {}^{40}K_{ill}(e^{\lambda t'} - 1)$$

450 We deduce the apparent K-Ar age  $t''$  of the mixing:

451 
$$t'' = \frac{1}{\lambda} \ln \left[ 1 + \left( \frac{{}^{40}K_{ms}}{{}^{40}K_{tot}} \right) (e^{\lambda t} - 1) + \left( \frac{{}^{40}K_{ill}}{{}^{40}K_{tot}} \right) (e^{\lambda t'} - 1) \right] \quad (VI-1)$$

452

453 where  ${}^{40}K_{ms}$  is the  ${}^{40}K$  content of muscovite,  ${}^{40}K_{ill}$  is the  ${}^{40}K$  content of illite,  ${}^{40}K_{tot}$  is the  ${}^{40}K$   
 454 content of the mixture,  $t$  is the K-Ar hydrothermal age of the muscovite,  $t'$  is the K-Ar age of  
 455 the illitization event and  $\lambda$  is the total  ${}^{40}K$  decay constant (here  $5.544 \times 10^{-10} \text{ yr}^{-1}$  after Steiger  
 456 & Jäger, **1977**).

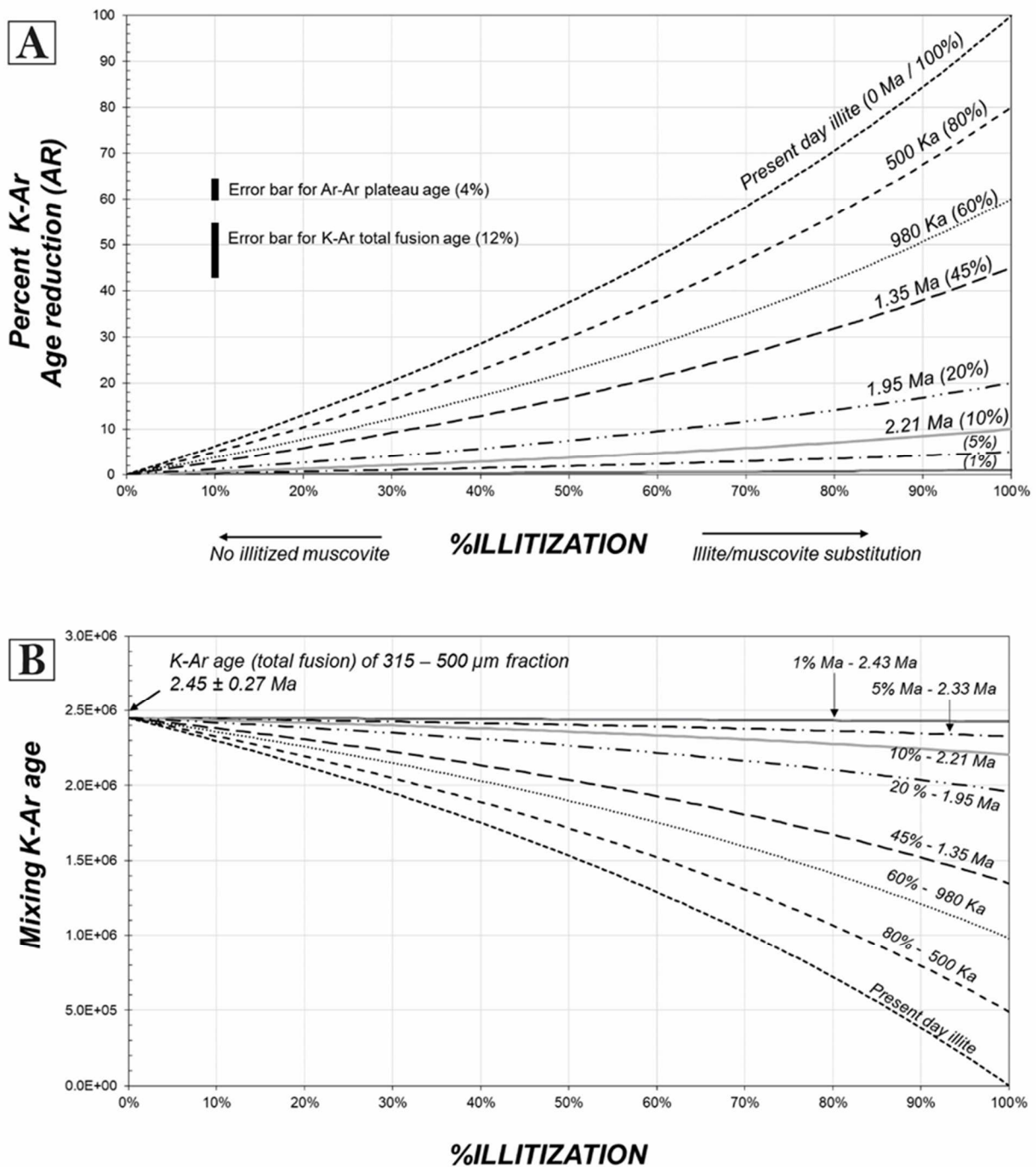
457 The % of K-Ar age reduction AR is defined as:

458 
$$AR = \frac{t - t''}{t} \quad (VI-2)$$

459

460 The  ${}^{40}K_{ms}/{}^{40}K_{tot}$  and  ${}^{40}K_{ill}/{}^{40}K_{tot}$  ratios in equation (VI-1) are calculated with  $M_{ms} = 398.71$   
 461  $\text{g}\cdot\text{mol}^{-1}$ ,  $M_{ill} = 389.34 \text{ g}\cdot\text{mol}^{-1}$ , weight % of  $\text{K}_2\text{O}_{ms} = 11.81\%$ , and that of  $\text{K}_2\text{O}_{ill} = 7.26\%$ . The  $t$   
 462 value in equation (VI-2) is the K-Ar age of the muscovite, i.e., the total fusion age of the  
 463 combined Ar-Ar experiments ( $2.45 \pm 0.27 \text{ Ma}$ , see Table A.3 in the online supplementary  
 464 data).

465 According to the modelling of Verati and Jourdan (**2014**), the variable parameters in our  
 466 study are the age of the illite ( $t'$ ) and the amount of illitization. In Figure 10, we plot eight  
 467 curves (different time spans between muscovite crystallization and illitization) showing the  
 468 %AR versus the % of illitization. The age difference between muscovite crystallization and  
 469 illitization is the main parameter influencing the calculated K-Ar age reduction (Fig. 10).  
 470 Regardless of the amount of illitization (the  $2\sigma$  error of the K-Ar age is larger than the time  
 471 span), if the time span between illitization and muscovite ranges between 0 and 10%, the  
 472 decrease in the K-Ar age is not significant enough to provide a mixing K-Ar age discordant  
 473 from the muscovite age. This result implies a fast cooling rate ( $>150^\circ\text{C}/200 \text{ ka}$ ) for the  
 474 Saintes hydrothermal system.  
 475



476  
477 Figure 10: A) Age reduction parameter (%AR) vs. % muscovite illitization. The curves are  
478 calculated for different  $t'$  (age of illitization). The muscovite age  $t$  = the K-Ar total fusion age of  
479  $2.45 \pm 0.27$  Ma (see text for explanation). The age of the illitization (% time span/muscovite)  
480 is specified for each curve. Error bars for K-Ar total fusion and Ar-Ar plateau age are reported  
481 (after error at  $2\sigma$  in Table A.3 in online supplementary data). B) Theoretical mixing K-Ar age vs.  
482 % muscovite illitization. K-Ar age of  $2.45 \pm 0.27$  Ma for the 315-500  $\mu\text{m}$  fraction is reported.  
483 Different theoretical curves are defined according to different ages for illitization (2.43 Ma to  
484 present day). For example, muscovite at 2.45 Ma displays an apparent K-Ar of 2.0 Ma with  
485 50% illitization occurring at 1.35 Ma. **[Black and White]**  
486

487 For a difference in age of 20% to 100% between muscovite crystallization and illitization, the  
488 related %AR remains low (<40%) for a high percent of alteration of 50%. High amounts of



489 illitization (70 – 90%) do not totally reset the muscovite age regardless of the time span  
490 between crystallization and illitization.

491  
492 **5.3. Les Saintes cooling rate in the tectonic framework of the Lesser Antilles arc**

493 The intra-oceanic subduction of the North-American plate beneath the Caribbean plate drives  
494 the Lesser Antilles magmatic arc (Martin-Kaye, 1969; Bouysse and Westerkamp, 1990) and  
495 the oblique convergence between these two plates is accommodated by crustal-scale strain  
496 partitioning and development of trench parallel extension (Feuillet et al., 2001, 2002). In this  
497 context the Guadeloupe archipelago is affected by a transtensive regime with development  
498 of both normal and strike-slip faults (Feuillet et al., 2002; Calcagno et al., 2012; Mathieu et  
499 al., 2013). Such a framework is favourable for significant and fast vertical movements in the  
500 arc crust (see discussions in Feuillet et al., 2004; Münch et al., 2013; Leclerc et al., 2016;  
501 Verati et al., 2018). The fast cooling rate obtained for Les Saintes hydrothermal system is  
502 consistent with this tectonic pattern and emphasizes also rapid exhumation of some pieces  
503 of the shallow arc crust under significant extension and erosion rates.

504  
505 **5.4. Implications for the duration of geothermal systems in magmatic arcs**

506 The combined plateau age at  $2.59 \pm 0.12$  Ma at  $2\sigma$  is the best age estimate of the high  
507 temperature hydrothermal system ( $>300^\circ\text{C}$ ) recognized on Terre-de-Haut Island. This age  
508 was obtained on a volcanic island for which other temporal constraints are available. We thus  
509 have the opportunity to test the robustness of our chronological results by a comparison with  
510 the ages obtained for volcanic activity on this island (emplacement of lava flows, volcanic  
511 domes or plugs, Fig. 1-B). Indeed, as highlighted in Fig.1-C hydrothermal transformations are  
512 gradually developed according to the finite deformation gradient observed in the field. As a  
513 consequence of this heterogeneous strain pattern, various volcanic formations are  
514 progressively affected by the high-temperature hydrothermal transformations, and thus when  
515 we date a volcanic flow outside of a given hydrothermalised shear zone, we date the protolith  
516 of the altered formation and we obtained a “oldest” limit for the geothermal activity. Of  
517 course, because we cannot identify all the volcanic protoliths involved in the highly altered  
518 zone, we cannot definitely discard the possibility of an activity of the geothermal system  
519 before the oldest dated volcanic formation. A first dataset was obtained (Jacques *et al.*,  
520 **1984**) by the K/Ar technique on whole-rock samples but did not consider the impacts of  
521 hydrothermal and/or supergene alteration processes on the ages. However, the results  
522 obtained with this approach, in the whole Lesser Antilles arc, are now considered outdated  
523 because of significant K loss and Ar enrichment potentially associated with alteration (see  
524 discussion in Samper *et al.*, **2007, 2009**). A more recent dataset of K-Ar ages (Zami *et al.*,  
525 **2014**) was obtained by the unspiked K-Ar technique using measurements on the  
526 groundmass only from a selection of fresh rocks, as proposed by Samper *et al.* (**2007, 2009**).  
527 Thus, the volcanic activity of Terre de Haut Island has been bracketed between  $2.98 \pm 0.04$   
528 Ma and  $2.00 \pm 0.03$  Ma. Within this framework, the hydrothermal study area is intruded by  
529 several volcanic plugs and domes (Fig. 1-B). In addition, these intrusive volcanic plugs and  
530 domes are totally unaltered and are thus not affected by hydrothermal alteration. Among  
531 these unaltered volcanic intrusives, the “Chameau” volcanic dome is dated at  $2.00 \pm 0.03$  Ma  
532 (Fig. 1-B, Zami *et al.*, **2014**). This age represents the uppermost or youngest limit for the  
533 activity of the hydrothermal system.

534 However using this result in order to approach the duration of the studied geothermal system  
535 implies to assume that the heat flow has remained stable through the geothermal history of  
536 Guadeloupe archipelago. The present-day conductive geothermal gradient was measured  
537 around the Guadeloupe archipelago in the range  $69.3 \pm 1.5$  and  $98.2 \pm 8.8$  °C/km (Manga et  
538 al., 2012). As demonstrated by recent mineralogical, petrological and geochronological  
539 investigations on the oldest hydrothermal metamorphic meta-volcanites recognized in this  
540 archipelago, this conductive gradient did not change during the last 5 Ma (Verati et al., 2018;  
541 Favier et al., 2019; Favier et al., 2021). We can therefore reasonably consider a stable heat  
542 flow over this time span. This assumption is consistent with the fact that the regional stress  
543 field also has remained unchanged since 5 Ma in the Guadeloupe archipelago (Feuillet et al.,

544 2002, 2004; Mathieu et al., 2011; Corsini et al., 2011; Lardeaux et al., 2013; Münch et al.,  
545 2013; Leclerc et al., 2016). However, during the operation of a given geothermal system,  
546 quick spurs of heat from deep below can always be considered. In a companion paper  
547 (Favier et al., 2021), we modelled the P-T stability fields of all the expected mineral  
548 assemblages for the studied chemical system. Under constant pressure, at 400°C, titanite is  
549 replaced by rutile, and epidote is replaced by zoisite, while and at around 480°C, muscovite  
550 disappears and biotite, cordierite and rutile are diagnostic phases. We never observed such  
551 mineral reactions in Terre-de-Haut hydrothermal zone. We can therefore discard the  
552 hypothesis of quick heat pulses leading development of higher thermal conditions. Of course,  
553 if such pulses lead development of constant temperature conditions, similar mineral  
554 assemblages are expected to crystallize and it will be impossible, by mineral and petrologic  
555 investigations, to distinguish these incremental heat inputs in a steady-state stable thermal  
556 gradient.

557 Taking into account all the assumptions presented and discussed in previous paragraphs,  
558 our new results are clearly consistent with the age database obtained by Zami *et al.* (2014),  
559 and the following points must be emphasized:

560 - First, the development of the studied hydrothermal system, regarded as an analogue of a  
561 high temperature geothermal system, was coeval with the volcanic activity on this island.

562 - Second, overall, the whole temporal dataset allows us to estimate a maximal duration of  
563 650 ka (i.e., the time difference between the hydrothermal event dated at  $2.59 \pm 0.12$  Ma,  
564 and the intrusion of the unaltered “Chameau” volcanic dome dated at  $2.00 \pm 0.03$  Ma) for the  
565 Saintes hydrothermal system.

566 To test the robustness of this result, it is quite interesting to compare it to the age well-know  
567 active geothermal system of Bouillante Bay (west coast of Guadeloupe, Bouchot et al., 2010;  
568 Thinon et al., 2010). The  $^{40}\text{Ar}/^{39}\text{Ar}$  dating of this high-enthalpy geothermal system, based on  
569 an adularia bearing hydrothermal breccia, indicates that the geothermal activity archipelago,  
570 still active, started at least  $248.2 \pm 50.2$  ka ago (Verati et al., 2014). Moreover, the estimated  
571 duration of the studied hydrothermal system is in agreement with the few available lifetimes  
572 obtained for other volcanic geothermal provinces or epithermal deposits located worldwide  
573 where hydrothermal activity ranges between a few hundred thousand years and a million  
574 years (Faure, 1986; Deloule & Turcotte, 1989; Nakai *et al.*, 1993; Barnes, 1997; Rowland &  
575 Sibson, 2004; Grimes et al., 1998 ; Velador et al., 2010). Last the proposed operating  
576 duration for the Saintes hydrothermal system, is also in agreement with thermal modelling of  
577 convective hydrothermal systems around shallow magmatic intrusions completed within tens  
578 of thousands of years to almost 1 Ma (Carslaw and Jaeger, 1959; Jaeger, 1959, 1968;  
579 Delaney, 1982; Kissling, 1999; Eldursi et al., 2009; Carrichi et al., 2012; Hoinkes et al.,  
580 2005).

581 This dating approach could also be carried out on younger geothermal systems (< 300 ka)  
582 that are of particular interest for geothermal exploration in active volcanic systems. The most  
583 important constraint on obtaining ages with the stepwise heating technique or total fusion  
584 analyses on multigrain separates is to evaluate the minimal masses of required material to  
585 detect enough radiogenic  $^{40}\text{Ar}$  in the samples. Dating such young geothermal materials is  
586 challenging because of the high content of atmospheric  $^{40}\text{Ar}$  compared to radiogenic  $^{40}\text{Ar}$ . In  
587 particular, we observe that Les Saintes metapyroxenes display a high atmospheric  
588 contamination with a mean value at 60%. Unfortunately, for young samples, error  
589 magnification begins to dominate when the proportion of radiogenic  $^{40}\text{Ar}$  is less than about  
590 10% of the total  $^{40}\text{Ar}$  and increase exponentially (McDougall and Harrison, 1999). In such  
591 case, taking into account (1) the K-content of metapyroxenes, (2) the atmospheric  $^{40}\text{Ar}$   
592 contribution of such hydrothermal minerals and (3) the detection limits of the most recent  
593 multicollector mass spectrometers, we estimate for a 300 ka old sample that a minimum of  
594 10 mg and 100 mg are required for total fusion on multigrain aliquots and stepwise heating  
595 analyses respectively (Fig. A-1).

596  
597

## 6. Conclusions

598 1. We confirm that, even for complex reaction microstructures, the  $^{40}\text{Ar}/^{39}\text{Ar}$  method, coupled  
599 with a high-resolution mineralogical analysis, is a powerful technique for dating high  
600 temperature hydro/geothermal systems. Under temperatures ranging from 400-200°C, the  
601 degree of crystallinity of K-bearing phases is a key parameter for accurate Ar-Ar dating,  
602 especially for muscovite.

603 2. Muscovites from hydrothermally altered pyroxenes with high crystallinity indexes and less  
604 than 40% illitization can provide accurate Ar-Ar plateau ages of crystallization for  
605 temperatures above 300°C. Illitization can have a fundamental impact on the Ar-Ar and K-Ar  
606 systematics only if the muscovite is highly illitized and/or if the illitization is much younger  
607 than the muscovite crystallization.

608 3. We report the first example of dating hydrothermal muscovite crystallization developed at  
609 the expense of meta-pyroxenes within transformed arc-related calc-alkaline volcanic rocks.  
610 This approach allows us to propose an age of  $2.59 \pm 0.12$  Ma for the development of the  
611 Terre-de-Haut fossil geothermal reservoir, with a maximal lifetime estimated at 650 ka.

612 4. Our modelling implies a fast cooling rate ( $>150^\circ\text{C}/200$  ka) for the Saintes hydrothermal  
613 system. This cooling rate has significant consequences for the stability and preservation of  
614 high temperature hydrothermal mineral phases over time. This first cooling rate estimate  
615 deserves to be challenged by dating other K-bearing hydrothermal minerals developed under  
616 lower temperature hydrothermal activity, such as jarosite, which is potentially present in the  
617 area of interest.

618

619

## 7. Acknowledgments

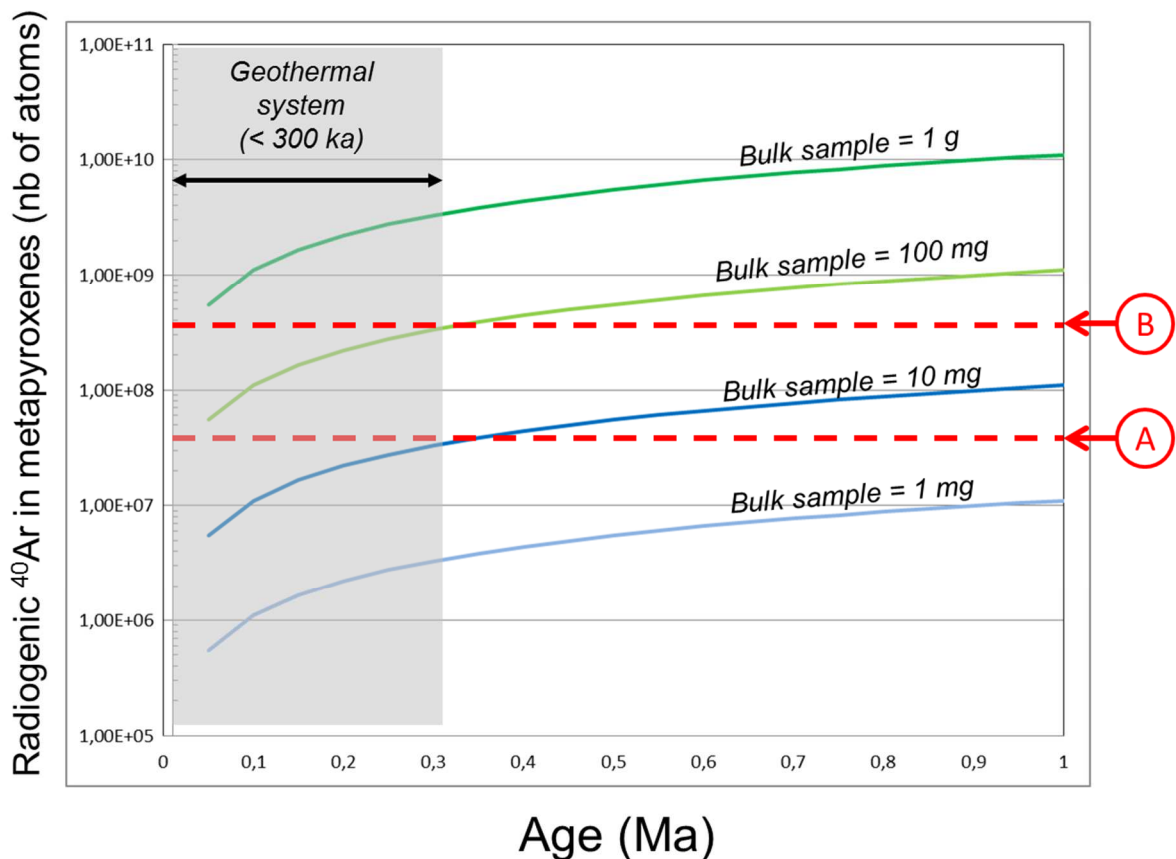
620 This paper is a contribution to the GEOTREF program, funded by the French government  
621 with the "Investissements d'Avenir" program and tutored by ADEME. We thank the  
622 researchers from the GEOTREF consortium for greatful discussions during the fieldwork  
623 campaigns in Guadeloupe and during scientific meetings. The authors thank Arthur Iemmolo  
624 for his technical support during  $^{40}\text{Ar}/^{39}\text{Ar}$  analysis, Magali Bonnefoy and Matthieu Zanti for  
625 sampling preparation, Gabriel Monge for his welcome to CEMEF for the use of the X-ray  
626 Diffraction device, Emile Voitus for his participation in the fieldwork campaigns and to the  
627 residents of the Terre-de-Haut Island. CCMA electron microscopy equipments have been  
628 funded by the Région Sud - Provence-Alpes-Côte d'Azur, the Conseil Départemental des  
629 Alpes Maritimes, and the GIS-IBISA. Finally, we are grateful to Pr. Balz Kamber for editorial  
630 work and to two anonymous reviewers for their useful thoughts and constructive reviews  
631 which improved the manuscript.

632

633

## 8. Appendices

634



635  
 636 Figure A.1 - Blue and green curves correspond to the amount of cumulated  
 637 radiogenic  $^{40}\text{Ar}$  with time ( $< 1$  Ma) in 1 mg, 10 mg, 100 mg and 1g of metaproxene  
 638 bulk sample respectively ( $\text{K}_2\text{O} = 11.82$  wt%;  $^{40}\text{K}/\text{K}_{\text{tot}} = 0,0001167$ ;  $\lambda = 5.544\text{E}^{-10} \text{ yr}^{-1}$ ;  
 639  $\lambda\varepsilon = 5.81\text{E}^{-11} \text{ yr}^{-1}$ ;  $N_A = 6.022 \times 10^{23} \text{ mol}^{-1}$ ).

640 Red lines represent the analytical detection limits for mass spectrometer (ARGUS  
 641 VI), i.e lines below which  $^{40}\text{Ar}$  can no longer be detected against the background  
 642 signal. Line A is related to total fusion experiment on multigrain aliquots, which must  
 643 be repeated at least 10 times to obtain an inverse isochron. Line B is related to  
 644 stepwise heating technique on a single aliquot (10 steps) which provides Ar-Ar  
 645 spectra. Calculations were made according to: (1) measurements were carried out in  
 646 multi-collection mode using Faraday cups equipped with  $10^{12}$  ohm, (2) the acquisition  
 647 time for each step is 600 seconds, (3) sensitivity was estimated knowing that a signal  
 648 of 1 fA ( $10^{-15}$  A) corresponds to a rate of 6000 ions per seconds, (3) the measured  
 649  $^{40}\text{Ar}$  peak must be five times higher than the monitored blanks.

650 For example, we can estimate for a 300 ka old sample that a minimum of 10 mg and  
 651 100 mg are required for total fusion on multigrain aliquots and stepwise heating  
 652 analyses respectively. For a 200 ka old sample 100 mg are required for total fusion  
 653 technique, and 1 g for step heating technique.

654  
 655  
 656 Table A.1 – Electron microprobe analyses and structural formula of high-temperature  
 657 hydrothermal phases [**Supplemental file: Excel file version**]

Mineral analysis number	Illite-Smectite															
	1 / 1 .	3 / 1 .	4 / 1 .	5 / 1 .	9 / 1 .	10 / 1 .	14 / 1 .	27 / 1 .	15 / 1 .	31 / 1 .	32 / 1 .	35 / 1 .	37 / 1 .	45 / 1 .	46 / 1 .	41 / 1 .
<b>Element (%wt oxide)</b>																
Al2O3	29.94	27.44	24.62	26.14	28.18	26.20	26.10	29.84	27.03	27.48	28.15	29.55	24.73	24.48	23.31	29.26
SiO2	45.55	41.51	36.88	41.59	43.51	43.05	40.07	43.79	41.66	39.69	41.78	42.79	40.01	39.45	39.11	42.76
TiO2	0.09	0.08	0.07	0.09	0.06	0.06	0.09	0.04	0.09	0.03	0.03	0.02	0.02	0.14	0.16	0.03
Na2O	0.08	0.05	0.03	0.03	0.07	0.03	0.03	0.10	0.04	0.06	0.11	0.09	0.03	0.02	0.03	0.09
MgO	9.42	11.88	19.28	14.57	9.57	8.53	14.04	10.24	12.18	16.50	10.59	7.92	19.18	15.24	13.65	10.57
MnO	0.82	0.76	1.28	0.98	0.65	0.55	1.08	0.65	0.97	0.90	0.64	0.48	0.90	1.12	1.23	0.52
FeO	0.94	1.70	2.81	1.96	1.34	1.33	1.77	1.21	1.53	1.69	1.34	0.98	1.96	2.04	1.79	1.21
K2O	6.51	5.19	2.20	3.33	6.00	6.64	3.68	3.93	4.58	3.70	3.46	6.04	1.17	3.85	3.99	3.79
CaO	0.21	0.26	0.37	0.38	0.30	0.25	0.31	0.34	0.28	0.31	0.45	0.26	0.66	0.30	0.38	0.53
<b>Total</b>	<b>93.56</b>	<b>88.88</b>	<b>87.53</b>	<b>89.07</b>	<b>89.68</b>	<b>86.64</b>	<b>87.18</b>	<b>90.14</b>	<b>88.35</b>	<b>90.36</b>	<b>86.54</b>	<b>88.12</b>	<b>88.64</b>	<b>86.65</b>	<b>83.65</b>	<b>88.76</b>
<b>Structural formula</b>																
Al	2.36	2.29	2.11	2.17	2.33	2.24	2.22	2.41	2.26	2.26	2.37	2.47	2.05	2.11	2.08	2.41
Si	3.05	2.94	2.68	2.93	3.05	3.13	2.89	3.01	2.96	2.77	2.99	3.03	2.82	2.88	2.96	2.98
Ti	0.00	0.00	0.00	0.01	0.00	0.00	0.01	0.00	0.00	0.00	0.00	0.00	0.00	0.01	0.01	0.00
Na	0.01	0.01	0.00	0.00	0.01	0.00	0.00	0.01	0.01	0.01	0.01	0.01	0.01	0.00	0.00	0.01
Mg	0.94	1.26	2.09	1.53	1.00	0.92	1.51	1.05	1.29	1.72	1.13	0.84	2.01	1.66	1.54	1.10
Mn	0.05	0.05	0.08	0.06	0.04	0.03	0.07	0.04	0.06	0.05	0.04	0.03	0.05	0.07	0.08	0.03
Fe	0.05	0.10	0.17	0.12	0.08	0.08	0.11	0.07	0.09	0.10	0.08	0.06	0.12	0.12	0.11	0.07
K	0.56	0.47	0.20	0.30	0.54	0.62	0.34	0.34	0.41	0.33	0.32	0.55	0.11	0.36	0.38	0.34
Ca	0.02	0.02	0.03	0.03	0.02	0.02	0.02	0.02	0.02	0.02	0.03	0.02	0.05	0.02	0.03	0.04
<b>Total (cation)</b>	<b>7.04</b>	<b>7.14</b>	<b>7.37</b>	<b>7.13</b>	<b>7.06</b>	<b>7.06</b>	<b>7.16</b>	<b>6.96</b>	<b>7.11</b>	<b>7.26</b>	<b>6.98</b>	<b>7.01</b>	<b>7.21</b>	<b>7.24</b>	<b>7.19</b>	<b>6.98</b>
<b>O (fixed)</b>	<b>11</b>	<b>11</b>	<b>11</b>	<b>11</b>	<b>11</b>	<b>11</b>	<b>11</b>	<b>11</b>	<b>11</b>	<b>11</b>	<b>11</b>	<b>11</b>	<b>11</b>	<b>11</b>	<b>11</b>	<b>11</b>

658  
659

Mineral analysis number	Illites								
	25 / 1 .	26 / 1 .	13 / 1 .	2 / 1 .	16 / 1 .	22 / 1 .	23 / 1 .	15	34 / 1 .
<b>Element (%wt oxide)</b>									
Al2O3	32.65	31.72	29.34	31.46	30.78	35.00	34.94	23.76	31.41
SiO2	48.10	47.53	46.90	48.16	48.63	50.51	49.31	51.97	45.63
TiO2	0.03	0.04	0.09	0.10	0.08	0.01	0.03	0.00	0.07
Na2O	0.16	0.14	0.09	0.08	0.08	0.19	0.22	0.00	0.06
MgO	4.44	4.97	4.95	4.97	4.32	0.97	1.06	0.84	3.74
MnO	0.29	0.34	0.27	0.26	0.21	0.03	0.02	0.00	0.19
FeO	0.61	0.73	0.70	0.63	0.87	0.22	0.27	7.93	0.45
K2O	6.17	6.93	7.42	9.07	8.42	7.59	6.64	4.89	7.85
CaO	0.29	0.24	0.21	0.13	0.17	0.19	0.32	0.00	0.19
<b>Total</b>	<b>92.74</b>	<b>92.64</b>	<b>89.99</b>	<b>94.87</b>	<b>93.56</b>	<b>94.72</b>	<b>92.79</b>	<b>89.39</b>	<b>89.58</b>
<b>Structural formula</b>									
Al	2.55	2.50	2.39	2.45	2.42	2.67	2.71	1.96	2.57
Si	3.19	3.18	3.24	3.19	3.25	3.27	3.25	3.64	3.17
Ti	0.00	0.00	0.00	0.01	0.00	0.00	0.00	0.00	0.00
Na	0.02	0.02	0.01	0.01	0.01	0.02	0.03	0.00	0.01
Mg	0.44	0.50	0.51	0.49	0.43	0.09	0.10	0.09	0.39
Mn	0.02	0.02	0.02	0.01	0.01	0.00	0.00	0.00	0.01
Fe	0.03	0.04	0.04	0.03	0.05	0.01	0.01	0.46	0.03
K	0.52	0.59	0.65	0.77	0.72	0.63	0.56	0.44	0.70
Ca	0.02	0.02	0.02	0.01	0.01	0.01	0.02	0.00	0.01
<b>Total (cation)</b>	<b>6.80</b>	<b>6.87</b>	<b>6.89</b>	<b>6.97</b>	<b>6.90</b>	<b>6.72</b>	<b>6.69</b>	<b>6.59</b>	<b>6.89</b>
<b>O (fixed)</b>	<b>11</b>	<b>11</b>	<b>11</b>	<b>11</b>	<b>11</b>	<b>11</b>	<b>11</b>	<b>11</b>	<b>11</b>

660  
661

Mineral	Muscovite									
analysis number	3	4	5	18 / 1 .	30 / 1 .	33 / 1 .	6	10	12	14
<b>Element (%wt oxide)</b>										
Al <sub>2</sub> O <sub>3</sub>	28.59	28.94	29.31	32.44	33.19	32.43	28.69	28.75	28.52	29.35
SiO <sub>2</sub>	48.05	47.96	47.13	49.45	49.41	48.85	48.11	47.89	48.19	47.07
TiO <sub>2</sub>	0.06	0.01	0.09	0.04	0.07	0.10	0.05	0.07	0.07	0.12
Na <sub>2</sub> O	0.04	0.08	0.03	0.11	0.15	0.08	0.03	0.01	0.03	0.05
MgO	0.28	0.43	0.61	1.63	1.55	2.21	0.47	0.29	0.57	0.69
MnO	0.07	0.02	0.10	0.07	0.06	0.10	0.06	0.12	0.04	0.07
FeO	6.62	7.41	5.79	0.16	0.13	0.27	6.41	6.63	6.37	5.81
K <sub>2</sub> O	9.81	9.94	9.87	10.00	9.92	9.84	9.75	9.88	9.79	9.79
CaO	0.03	0.03	0.01	0.10	0.13	0.07	0.02	0.01	0.02	0.00
Total	93.55	94.82	92.94	93.99	94.60	93.96	93.59	93.65	93.60	92.95
<b>Structural formula</b>										
Al	2.33	2.34	2.40	2.54	2.58	2.54	2.33	2.34	2.32	2.40
Si	3.32	3.29	3.27	3.29	3.26	3.25	3.32	3.31	3.33	3.27
Ti	0.00	0.00	0.00	0.00	0.00	0.00	0.00	0.00	0.00	0.01
Na	0.01	0.01	0.00	0.01	0.02	0.01	0.00	0.00	0.00	0.01
Mg	0.03	0.04	0.06	0.16	0.15	0.22	0.05	0.03	0.06	0.07
Mn	0.00	0.00	0.01	0.00	0.00	0.01	0.00	0.01	0.00	0.00
Fe	0.38	0.42	0.34	0.01	0.01	0.01	0.37	0.38	0.37	0.34
K	0.87	0.87	0.87	0.85	0.83	0.84	0.86	0.87	0.86	0.87
Ca	0.00	0.00	0.00	0.01	0.01	0.01	0.00	0.00	0.00	0.00
Total (cation)	6.94	6.98	6.96	6.87	6.87	6.89	6.94	6.95	6.94	6.96
O (fixed)	11	11	11	11	11	11	11	11	11	11

662  
663

Mineral	Chlorite												
analysis number	28 / 1 .	24 / 1 .	36 / 1 .	17 / 1 .	19 / 1 .	21 / 1 .	1	7	8	9	11	13	2
<b>Element (%wt oxide)</b>													
Al <sub>2</sub> O <sub>3</sub>	23.10	23.77	23.49	25.72	25.70	24.60	20.30	20.18	20.08	20.22	20.11	20.27	20.57
SiO <sub>2</sub>	34.37	35.21	37.94	38.83	37.86	37.62	27.01	25.45	25.66	25.51	25.69	25.53	27.32
TiO <sub>2</sub>	0.05	0.03	0.03	0.00	0.06	0.03	0.06	0.01	0.00	0.00	0.01	0.02	0.01
Na <sub>2</sub> O	0.03	0.01	0.04	0.02	0.03	0.02	0.00	0.05	0.19	0.00	0.04	0.02	0.00
MgO	19.42	22.40	20.90	18.26	18.53	22.26	16.50	13.94	13.73	13.65	13.71	13.95	16.71
MnO	1.15	1.27	1.05	0.97	1.09	1.24	0.33	0.30	0.37	0.23	0.34	0.26	0.29
FeO	2.29	2.41	2.30	1.94	2.03	2.29	22.48	24.36	27.85	26.98	27.91	27.82	23.64
K <sub>2</sub> O	0.18	0.24	0.76	0.29	0.28	0.31	0.00	0.00	0.00	0.00	0.00	0.00	0.00
CaO	0.51	0.38	0.55	0.62	0.55	0.41	0.10	0.00	0.00	0.00	0.00	0.00	0.09
Total	81.10	85.71	87.06	86.65	86.12	88.78	86.78	84.29	87.88	86.59	87.81	87.87	88.63
<b>Structural formula</b>													
Al	2.68	2.62	2.54	2.76	2.78	2.05	2.50	2.60	2.53	2.57	2.53	2.55	2.49
Si	3.38	3.30	3.48	3.54	3.48	2.66	2.83	2.78	2.74	2.75	2.74	2.72	2.81
Ti	0.00	0.00	0.00	0.00	0.00	0.00	0.00	0.00	0.00	0.00	0.00	0.00	0.00
Na	0.01	0.00	0.01	0.00	0.00	0.00	0.00	0.01	0.04	0.00	0.01	0.00	0.00
Mg	2.85	3.13	2.86	2.48	2.54	2.35	2.57	2.27	2.19	2.19	2.18	2.22	2.56
Mn	0.10	0.10	0.08	0.07	0.08	0.07	0.03	0.03	0.03	0.02	0.03	0.02	0.03
Fe	0.19	0.19	0.18	0.15	0.16	0.14	1.97	2.23	2.49	2.43	2.49	2.48	2.03
K	0.02	0.03	0.09	0.03	0.03	0.03	0.00	0.00	0.00	0.00	0.00	0.00	0.00
Ca	0.05	0.04	0.05	0.06	0.05	0.03	0.01	0.00	0.00	0.00	0.00	0.00	0.01
Total (cation)	9.29	9.40	9.29	9.10	9.14	7.33	9.92	9.92	10.02	9.97	9.99	10.00	9.94
O (fixed)	14	14	14	14	14	14	14	14	14	14	14	14	14

664  
665

666 Table A.2 – XRD pattern decomposition

Sample	Position	Intensity	Area	FWHM	Interpretation
16STH19-1_AD 315-500 µm	5.81	10900.6	13177.4	1.14	Chlorite-Smectite (001)
	6.12	6828.17	1946.31	0.27	
	6.69	1939.5	195.95	0.15	Illite-Smectite [Illite-rich] ?
	8.67	2200.51	1229.94	0.53	Illite (001)
	8.80	3695.56	466.4	0.12	Mica (001)
	12.34	8267.05	2970.77	0.34	Chlorite (002)
	13.76	1294.95	353.38	0.26	Feldspar
	17.68	3442.68	1164.31	0.32	Illite-Mica (002)
18.64	3529.18	1370.53	0.36	Chlorite (003)	
16STH19-1_EG 315-500 µm	5.14	6569.07	4575.52	0.65	Smectite (001)
	6.09	5696.10	2019.63	0.33	Chlorite (001)
	8.72	1406.39	1054.28	0.7	Illite (001)
	8.8	3104.77	476.93	0.14	Mica (001)
	9.52	627.18	125.44	0.38	Smectite (002)
	12.25	3449.96	1846.5	0.5	Chlorite (002) [Chlorite-Smectite]
	12.37	3058.74	665.46	0.2	Chlorite (002) [Chlorite]
	13.81	986.34	186.23	0.18	Feldspar
	17.68	1393.94	388.12	0.26	Illite-Mica (002)
	18.65	2294.22	1024.21	0.42	Chlorite (003)

667  
668  
669

Table A.3 – Compiled Ar-Ar results **[Supplemental file: Excel files]**

	K-Ar total fusion (Ma)	2σ	Plateau age (Ma)	2σ	MSWD	% <sup>39</sup> Ar released	Isochron age (Ma)	2σ	<sup>40</sup> Ar/ <sup>36</sup> Ar i	2σ
315 - 500 µm fraction										
Experiments:										
#B7-B8	2.53	0.32	2.78	0.22	0.31	98%	2.77	0.33	299.9	12.6
#A9 A10	2.27	0.75	2.45	0.25	0.38	87%	2.59	0.31	292.6	9
#B12	2.57	0.25	2.62	0.2	0.33	99%	2.57	0.31	297.4	8.5
#B2	2.52	0.62	2.55	0.44	0.32	61%	2.88	1.54	277.2	109
Combined experiments	2.45	0.27	2.59	0.12	0.39	90%	2.67	0.17	295.9	5.5

670  
671

672  
673  
674  
675  
676  
677  
678  
679  
680  
681  
682  
683  
684  
685  
686  
687  
688  
689  
690  
691  
692  
693  
694  
695  
696  
697  
698  
699  
700  
701  
702  
703  
704  
705  
706  
707  
708  
709  
710  
711  
712  
  
713  
714  
715  
716  
  
717  
718  
  
719  
720

## 9. References

- AREHART, G., CHRISTENSON, B., WOOD, C., FOLAND, K., & BROWNE, P.R.. **2002**. Timing of volcanic, plutonic and geothermal activity at Ngatamariki, New Zealand. *Journal of Volcanology and Geothermal Research*, 116, 201–214, doi: 10.1016/S0377-0273(01)00315-8.
- ÁRKAI, P. **1991**. Chlorite crystallinity: an empirical approach and correlation with illite crystallinity, coal rank and mineral facies as exemplified by Palaeozoic and Mesozoic rocks of northeast Hungary. *Journal of Metamorphic Geology*, 9, 723–734, doi: 10.1111/j.1525-1314.1991.tb00561.x.
- ARNÓRSSON, S. **1995**. Geothermal systems in Iceland: Structure and conceptual models—I. High-temperature areas. *Geothermics*, 24, 561–602, doi: 10.1016/0375-6505(95)00025-9.
- BARCELONA, H., YAGUPSKY, D., VIGIDE, N., & SENGER, M. **2019**. Structural model and slip-dilation tendency analysis at the Copahue geothermal system: Inferences on the reservoir geometry. *Journal of Volcanology and Geothermal Research*, 375, 18–31, doi: 10.1016/j.jvolgeores.2019.03.007.
- BARNES, H.L. **1997**. *Geochemistry of Hydrothermal Ore Deposits*. John Wiley & Sons.
- BEAUCHAMPS, G., LEDÉSER, B., HÉBERT, R., NAVÉLOT, V., & FAVIER, A. **2019**. The characterisation of an exhumed high temperature paleo geothermal system on Terre de Haut Island ( the Les Saintes archipelago , Guadeloupe ) in terms of clay minerals and petrophysics. *Geothermal Energy*, 1–18, doi: 10.1186/s40517-019-0122-y.
- BERTANI, R. **2016**. Geothermal power generation in the world 2010–2014 update report. *Geothermics*, 60, 31–43, doi: 10.1016/j.geothermics.2015.11.003.
- BIBBY, H.M., CALDWELL, T.G., DAVEY, F.J., & WEBB, T.H. **1995**. Geophysical evidence on the structure of the Taupo Volcanic Zone and its hydrothermal circulation. *Journal of Volcanology and Geothermal Research*, 68, 29–58, doi: 10.1016/0377-0273(95)00007-H.
- BOUYASSE, P. & WESTERCAMP, D. **1990**. Subduction of Atlantic aseismic ridges and Late Cenozoic evolution of the Lesser Antilles island arc. *Tectonophysics*, 175, 349–380, doi: 10.1016/0040-1951(90)90180-G.
- BROCKAMP, O., CLAUER, N., & ZUTHER, M. **2003**. Authigenic sericite record of a fossil geothermal system: the Offenburg trough, central Black Forest, Germany. *International Journal of Earth Sciences*, 92, 843–851, doi: 10.1007/s00531-003-0368-1.
- BROWNE, P.R.L. **1978**. Hydrothermal alteration in active geothermal fields. *Annual Review of Earth and Planetary Sciences*, 6, 229–250.
- CARICCHI, L., ANNEN, C., RUST, A., & BLUNDY, J. **2012**. Insights into the mechanisms and timescales of pluton assembly from deformation patterns of mafic enclaves. *Journal of Geophysical Research: Solid Earth*, 117, n/a-n/a, doi: 10.1029/2012JB009325.
- CARLUT, J., QUIDELLEUR, X., COURTILLOT, V., & BOUDON, G. **2000**. Paleomagnetic directions and K/Ar dating of 0 to 1 Ma lava flows from La Guadeloupe Island (French West Indies): Implications for time-averaged field models. *Journal of Geophysical Research: Solid Earth*, 105, 835–849, doi: 10.1029/1999JB900238.
- CARSLAW, H.S. & JAEGER, J.C. **1959**. *Conduction of Heat in Solids*. London, Oxford Univ. Press.
- CHERKOSE, B.A. & MIZUNAGA, H. **2018**. Resistivity imaging of Aluto-Langano geothermal field using 3-D magnetotelluric inversion. *Journal of African Earth*



721 *Sciences*, 139, 307–318, doi: 10.1016/j.jafrearsci.2017.12.017.

722 CLAUER, N. **2013**. The K-Ar and  $^{40}\text{Ar}/^{39}\text{Ar}$  methods revisited for dating fine-grained  
723 K-bearing clay minerals. *Chemical Geology*, 354, 163–185, doi:  
724 10.1016/j.chemgeo.2013.05.030.

725 CLAUER, N., ZWINGMANN, H., LIEWIG, N., & WENDLING, R. **2012**. Comparative  
726  $^{40}\text{Ar}/^{39}\text{Ar}$  and K–Ar dating of illite-type clay minerals: A tentative explanation for  
727 age identities and differences. *Earth-Science Reviews*, 115, 76–96, doi:  
728 10.1016/j.earscirev.2012.07.003.

729 DALRYMPLE, G.B., GROVE, M., LOVERA, O.M., HARRISON, T.M., HULEN, J.B., &  
730 LANPHERE, M.A. **1999**. Age and thermal history of the Geysers plutonic complex  
731 (felsite unit), Geysers geothermal field, California: a  $^{40}\text{Ar}/^{39}\text{Ar}$  and U–Pb study.  
732 *Earth and Planetary Science Letters*, 173, 285–298, doi: 10.1016/S0012-  
733 821X(99)00223-X.

734 DELANEY, P.T. **1982**. Rapid intrusion of magma into wet rock: Groundwater flow due  
735 to pore pressure increases. *Journal of Geophysical Research: Solid Earth*, 87,  
736 7739–7756.

737 DELOULE, E. & TURCOTTE, D.L. **1989**. The flow of hot brines in cracks and the  
738 formation of ore deposits. *Economic Geology*, 84, 2217–2225, doi: doi:  
739 10.2113/gsecongeo.84.8.2217.

740 DONG, H., HALL, C.M., PEACOR, D.R., & HALLIDAY, A.N. **1995**. Mechanisms of Argon  
741 Retention in Clays Revealed by Laser  $^{40}\text{Ar}$ - $^{39}\text{Ar}$  Dating. *Science*, 267, 355–359,  
742 doi: 10.1126/science.267.5196.355.

743 DRITS, V., SRODON, J., & EBERL, D.D. **1997**. XRD Measurement of Mean Crystallite  
744 Thickness of Illite and Illite/Smectite: Reappraisal of the Kubler Index and the  
745 Scherrer Equation. *Clays and Clay Minerals*, 45, 461–475, doi:  
746 10.1346/CCMN.1997.0450315.

747 ELDURSI, K., BRANQUET, Y., GUILLOU-FROTTIER, L., & MARCOUX, E. **2009**. Numerical  
748 investigation of transient hydrothermal processes around intrusions: Heat-  
749 transfer and fluid-circulation controlled mineralization patterns. *Earth and*  
750 *Planetary Science Letters*, 288, 70–83, doi: 10.1016/j.epsl.2009.09.009.

751 FAURE, G. **1986**. *Principles of Isotope Geology*. New-York, John Wiley & Sons.

752 FAVIER, A. **2019**. *Evolution Spatio-Temporelle de l'hydrothermalisme Dans La Plaque*  
753 *Supérieure de l'arc Des Petites Antilles En Guadeloupe. Applications Aux*  
754 *Systèmes Géothermaux*. Université des Antilles, Pointe-à-Pitre, Guadeloupe.

755 FAVIER, A., LARDEAUX, J.-M., LEGENDRE, L., VERATI, C., PHILIPPON, M., CORSINI, M.,  
756 MÜNCH, P., & VENTALON, S. **2019**. Tectono-metamorphic evolution of shallow  
757 crustal levels within active volcanic arcs. Insights from the exhumed Basal  
758 Complex of Basse-Terre (Guadeloupe, French West Indies). *BSGF - Earth*  
759 *Sciences Bulletin*, 190, 22, doi: 10.1051/bsgf/2019011.

760 FAVIER, A., LARDEAUX, J.-M., CORSINI, M., VERATI, C., NAVELOT, V., GERAUD, Y.,  
761 DIRAISON, M., VENTALON, S., & VOITUS, E. **2021**. Characterization of an exhumed  
762 high-temperature hydrothermal system and its application for deep geothermal  
763 exploration: An example from Terre-de-Haut Island (Guadeloupe archipelago,  
764 Lesser Antilles volcanic arc). *Journal of Volcanology and Geothermal Research*,  
765 107256, doi: 10.1016/j.jvolgeores.2021.107256.

766 GOLDFARB, R., GROVES, D., & GARDOLL, S. **2001**. Orogenic gold and geologic time: a  
767 global synthesis. *Ore Geology Reviews*, 18, 1–75, doi: 10.1016/S0169-  
768 1368(01)00016-6.

769 GRIMES, S., RICKARD, D., HAWKESWORTH, C., VAN CALSTEREN, P., & BROWNE, P. **1998**.

770 A U–Th calcite isochron age from an active geothermal field in New Zealand.  
771 *Journal of Volcanology and Geothermal Research*, 81, 327–333, doi:  
772 10.1016/S0377-0273(98)00005-5.

773 GROVES, D., GOLDFARB, R., GEBRE-MARIAM, M., HAGEMANN, S., & ROBERT, F. **1998**.  
774 Orogenic gold deposits: A proposed classification in the context of their crustal  
775 distribution and relationship to other gold deposit types. *Ore Geology Reviews*,  
776 13, 7–27, doi: 10.1016/s0169-1368(97)00012-7.

777 GUILBERT, J.M. & PARK, C.F.J. **1986**. *The Geology of Ore Deposits*. New York, W. H.  
778 Freeman and Compagny.

779 HAINES, S.H. & VAN DER PLUIJM, B.A. **2008**. Clay quantification and Ar–Ar dating of  
780 synthetic and natural gouge: Application to the Miocene Sierra Mazatán  
781 detachment fault, Sonora, Mexico. *Journal of Structural Geology*, 30, 525–538,  
782 doi: 10.1016/j.jsg.2007.11.012.

783 HALL, C.M., HIGUERAS, P.L., KESLER, S.E., LUNAR, R., DONG, H., & HALLIDAY, A.N.  
784 **1997**. Dating of alteration episodes related to mercury mineralization in the  
785 Almadén district, Spain. *Earth and Planetary Science Letters*, 148, 287–298, doi:  
786 10.1016/S0012-821X(97)00041-1.

787 HAMES, W., UNGER, D., SAUNDERS, J., & KAMENOV, G. **2009**. Early Yellowstone  
788 hotspot magmatism and gold metallogeny. *Journal of Volcanology and  
789 Geothermal Research*, 188, 214–224, doi: 10.1016/j.jvolgeores.2009.07.020.

790 HEDENQUIST, J.W. & BROWNE, P.R.L. **1989**. The evolution of the Waiotapu geothermal  
791 system, New Zealand, based on the chemical and isotopic composition of its  
792 fluids, minerals and rocks. *Geochimica et Cosmochimica Acta*, 53, 2235–2257,  
793 doi: 10.1016/0016-7037(89)90347-5.

794 HEDENQUIST, J.W., ARRIBAS, A.J., & GONZALEZ-URIEN, E. **2000**. Exploration for  
795 epithermal gold deposits. *In: SEG Review*. 245–277.

796 HENLEY, R.W. & ELLIS, A.J. **1983**. Geothermal systems ancient and modern: a  
797 geochemical review. *Earth-Science Reviews*, 19, 1–50, doi: 10.1016/0012-  
798 8252(83)90075-2.

799 HOINKES, C., HAUZENBERGER, C.A., & SCHMID, R. **2005**. Metamorphic rocks -  
800 Classification, nomenclature and formation. *In: Selley, R. C., Cocks, R. & Plimer,  
801 I. R. (eds) Encyclopedia of Geology*. Academic Press, 386–402.

802 HOWARD, S.A. & PRESTON, K.D. **1989**. Profile fitting of powder diffraction patterns. *In:  
803 Modern Powder Diffraction*. 217–275.

804 INOUE, A. & KITAGAWA, R. **1994**. Morphological characteristics of illite clay minerals  
805 from a hydrothermal system. *American Mineralogist*, 79, 700–711.

806 INOUE, A., UTADA, M., & WAKITA, K. **1992**. Smectite-to-illite conversion in natural  
807 hydrothermal systems. *Applied Clay Science*, 7, 131–145, doi: 10.1016/0169-  
808 1317(92)90035-L.

809 ISIK, V., UYSAL, I.T., CAGLAYAN, A., & SEYITOGU, G. **2014**. The evolution of intraplate  
810 fault systems in central Turkey: Structural evidence and Ar–Ar and Rb–Sr age  
811 constraints for the Savcili Fault Zone. *Tectonics*, 33, 1875–1899, doi:  
812 10.1002/2014TC003565.

813 JACQUES, D. & MAURY, R.C. **1988**. Carte géologique au 1/20 000e, département de la  
814 Guadeloupe, Les Saintes. *BRGM, Service Géologique National, Orléans*.

815 JACQUES, D., MAURY, R.C., & BELLON, H. **1984**. *Geology and K–Ar geochronology of  
816 Les Saintes island, guadeloupe, French West-Indies Géologie et géochronologie  
817 40K–40Ar des îles des Saintes (Guadeloupe)*. Gauthier-Villars.

818 JAEGER, J.C. **1959**. Temperatures outside a cooling intrusive sheet. *American Journal  
819 of Science*, 257, 44–54, doi: 10.2475/ajs.257.1.44.

- 820 JAEGER, J.C. **1968**. Cooling and solidification of igneous rocks. *In*: Hess, H. H. &  
821 Poldervaart, A. (eds) *Basalts – The Poldervaart Treatise on Rocks of Basaltic*  
822 *Composition, Vol.2*. New-York, John Wiley, 503–536.
- 823 JI, J. & BROWNE, P.R.L. **2000**. Relationship between illite crystallinity and temperature  
824 in active geothermal systems of New Zealand. *Clays and Clay Minerals*, 48,  
825 139–144.
- 826 JOURDAN, F., MATZEL, J.P., & RENNE, P.R. **2007**. <sup>39</sup>Ar and <sup>37</sup>Ar recoil loss during  
827 neutron irradiation of sanidine and plagioclase. *Geochimica et Cosmochimica*  
828 *Acta*, 71, 2791–2808, doi: 10.1016/j.gca.2007.03.017.
- 829 KISSLING, W.M. **1999**. Modeling of cooling plutons in the Taupo Volcanic Zone New  
830 Zealand. *In*: *24th Workshop on Geothermal Reservoir Engineering*. Stanford,  
831 California, SGP-TR-162.
- 832 KOPPERS, A.A.P. **2002**. ArArCALC—software for <sup>40</sup>Ar/<sup>39</sup>Ar age calculations.  
833 *Computers & Geosciences*, 28, 605–619, doi: 10.1016/S0098-3004(01)00095-4.
- 834 KÜBLER, B. **1967**. La cristallinité de l'illite et les zones tout à fait supérieures du  
835 métamorphisme. *In*: *Étages Tectoniques, Colloque de Neuchâtel 1966*. La  
836 Baconniere, Neuchâte, 105–121.
- 837 LEE, J.-Y., MARTI, K., SEVERINGHAUS, J.P., KAWAMURA, K., H-S., Y., LEE, J.B., & KIM,  
838 J.S. **2006**. A redetermination of the isotopic abundances of atmospheric Ar.  
839 *Geochimica et Cosmochimica Acta*, 4507–4512.
- 840 MÁRTON, I., MORITZ, R., & SPIKINGS, R. **2010**. Application of low-temperature  
841 thermochronology to hydrothermal ore deposits: Formation, preservation and  
842 exhumation of epithermal gold systems from the Eastern Rhodopes, Bulgaria.  
843 *Tectonophysics*, 483, 240–254, doi: 10.1016/j.tecto.2009.10.020.
- 844 MERRIMAN, R.J. & PEACOR, D.R. **1998**. Very Low-Grade Metapelites: Mineralogy,  
845 Microfabrics and Measuring Reaction Progress. *In*: *Low-Grade Metamorphism*.  
846 Oxford, UK, Blackwell Publishing Ltd., 10–60., doi:  
847 10.1002/9781444313345.ch2.
- 848 MEYER, C. & HEMLEY, J.J. **1967**. Wall rock alteration. *In*: *Geochemistry of*  
849 *Hydrothermal Ore Deposits*. New-York, 166–235.
- 850 MILICICH, S.D., CHAMBEFORT, I., WILSON, C.J.N., ALCARAZ, S., IRELAND, T.R.,  
851 BARDSLEY, C., & SIMPSON, M.P. **2020**. A zircon U-Pb geochronology for the  
852 Rotokawa geothermal system, New Zealand, with implications for Taupō  
853 Volcanic Zone evolution. *Journal of Volcanology and Geothermal Research*, 389,  
854 106729, doi: 10.1016/j.jvolgeores.2019.106729.
- 855 NAKAI, S., HALLIDAY, A.N., KESLER, S.E., JONES, H.D., KYLE, J.R., & LANE, T.E. **1993**.  
856 Rb-Sr dating of sphalerites from Mississippi Valley-type (MVT) ore deposits.  
857 *Geochimica et Cosmochimica Acta*, 57, 417–427, doi: 10.1016/0016-  
858 7037(93)90440-8.
- 859 NAVELOT, V., GERAUD, Y., FAVIER, A., DIRAISON, M., CORSINI, M., LARDEAUX, J.-M.,  
860 VERATI, C., MERCIER DE LEPINAY, J., LEGENDRE, L., & BEAUCHAMPS, G. **2018**.  
861 Petrophysical properties of volcanic rocks and impacts of hydrothermal alteration  
862 in the Guadeloupe Archipelago (West Indies). *Journal of Volcanology and*  
863 *Geothermal Research*, 360, 1–21, doi: 10.1016/j.jvolgeores.2018.07.004.
- 864 OLIVEROS, VER., AGUIRRE, L., MORATA, D., SIMONETTI, A., VERGARA, M., BELMAR, M., &  
865 CALDERÓN, S. **2008**. Geochronology of very low-grade Mesozoic Andean  
866 metabasites; an approach through the K–Ar, <sup>40</sup>Ar/<sup>39</sup>Ar and U–Pb LA-MC-ICP-  
867 MS methods. *Journal of the Geological Society*, 165, 579–584, doi:  
868 10.1144/0016-76492007-113.

- 869 OZE, C., CATTELL, H., & GROVE, M. **2017**. 40 Ar/ 39 Ar dating and thermal modeling of  
870 adularia to constrain the timing of hydrothermal activity in magmatic settings.  
871 *Geology*, 45, 43–46, doi: 10.1130/G38405.1.
- 872 RAGNARSSON, A. **2015**. Geothermal development in Iceland 2010–2014. *In*:  
873 *Proceedings World Geothermal Congress 2015*. Melbourne, Australia, 15.
- 874 RENNE, P.R., MUNDIL, R., BALCO, G., MIN, K., & LUDWIG, K.R. **2010**. Joint  
875 determination of 40K decay constants and 40Ar\*/40K for the Fish Canyon  
876 sanidine standard, and improved accuracy for 40Ar/39Ar geochronology.  
877 *Geochimica et Cosmochimica Acta*, 74, 5349–5367, doi:  
878 10.1016/j.gca.2010.06.017.
- 879 RICCI, J., LAHITTE, P., & QUIDELLEUR, X. **2015a**. Construction and destruction rates of  
880 volcanoes within tropical environment: Examples from the Basse-Terre Island  
881 (Guadeloupe, Lesser Antilles). *Geomorphology*, 228, 597–607, doi:  
882 10.1016/j.geomorph.2014.10.002.
- 883 RICCI, J., QUIDELLEUR, X., & LAHITTE, P. **2015b**. Volcanic evolution of central Basse-  
884 Terre Island revisited on the basis of new geochronology and geomorphology  
885 data. *Bulletin of Volcanology*, 77, 84, doi: 10.1007/s00445-015-0970-7.
- 886 RICCI, J., QUIDELLEUR, X., PALLARES, C., & LAHITTE, P. **2017**. High-resolution K-Ar  
887 dating of a complex magmatic system: The example of Basse-Terre Island  
888 (French West Indies). *Journal of Volcanology and Geothermal Research*, 345,  
889 142–160, doi: 10.1016/j.jvolgeores.2017.07.013.
- 890 ROSENBERG, M.D., WILSON, C.J.N., BIGNALL, G., IRELAND, T.R., SEPULVEDA, F., &  
891 CHARLIER, B.L.A. **2020**. Structure and evolution of the Wairakei–Tauhara  
892 geothermal system (Taupo Volcanic Zone, New Zealand) revisited with a new  
893 zircon geochronology. *Journal of Volcanology and Geothermal Research*, 390,  
894 106705, doi: 10.1016/j.jvolgeores.2019.106705.
- 895 ROWLAND, J. V. & SIBSON, R.H. **2004**. Structural controls on hydrothermal flow in a  
896 segmented rift system, Taupo Volcanic Zone, New Zealand. *Geofluids*, 4, 259–  
897 283, doi: 10.1111/j.1468-8123.2004.00091.x.
- 898 SAMPER, A., QUIDELLEUR, X., LAHITTE, P., & MOLLEX, D. **2007**. Timing of effusive  
899 volcanism and collapse events within an oceanic arc island: Basse-Terre,  
900 Guadeloupe archipelago (Lesser Antilles Arc). *Earth and Planetary Science  
901 Letters*, 258, 175–191, doi: 10.1016/j.epsl.2007.03.030.
- 902 SAMPER, A., QUIDELLEUR, X., KOMOROWSKI, J.-C., LAHITTE, P., & BOUDON, G. **2009**.  
903 Effusive history of the Grande Découverte Volcanic Complex, southern Basse-  
904 Terre (Guadeloupe, French West Indies) from new K–Ar Cassignol–Gillot ages.  
905 *Journal of Volcanology and Geothermal Research*, 187, 117–130, doi:  
906 10.1016/j.jvolgeores.2009.08.016.
- 907 SASADA, M., TAGUCHI, S., & HEDENQUIST, J.W. **2000**. Japanese geothermal systems  
908 developments in the 1990s-Preface. *Geothermics*, 29, 123–126.
- 909 STEIGER, R.H. & JÄGER, E. **1977**. Subcommittee on geochronology: Convention on  
910 the use of decay constants in geo- and cosmochronology. *Earth and Planetary  
911 Science Letters*, 36, 359–362, doi: 10.1016/0012-821X(77)90060-7.
- 912 VELADOR, J.M., HEIZLER, M.T., & CAMPBELL, A.R. **2010**. Timing of Magmatic Activity  
913 and Mineralization and Evidence of a Long-Lived Hydrothermal System in the  
914 Fresnillo Silver District, Mexico: Constraints from 40Ar/39Ar Geochronology.  
915 *Economic Geology*, 105, 1335–1349, doi: 10.2113/econgeo.105.7.1335.
- 916 VELDE, B. **1985**. *A Physico-Chemical Explanation of Their Occurrence*.

- 917 *Developments in Sedimentology*. Amsterdam, Elsevier.
- 918 VERATI, C. & JOURDAN, F. **2014**. Modelling effect of sericitization of plagioclase on the  
919 40 K/ 40 Ar and 40 Ar/ 39 Ar chronometers: implication for dating basaltic rocks  
920 and mineral deposits. *Geological Society, London, Special Publications*, 378,  
921 155–174, doi: 10.1144/SP378.14.
- 922 VERATI, C., PATRIER-MAS, P., LARDEAUX, J.-M., & BOUCHOT, V. **2014**. Timing of  
923 geothermal activity in an active island-arc volcanic setting: First 40Ar/39Ar dating  
924 from Bouillante geothermal field (Guadeloupe, French West Indies). *Geological  
925 Society, London, Special Publications*, 378, 285–295, doi: 10.1144/SP378.19.
- 926 VERATI, C., MAZABRAUD, Y., LARDEAUX, J.-M., CORSINI, M., SCHNEIDER, D., VOITUS, E.,  
927 & ZAMI, F. **2016**. Tectonic evolution of Les Saintes archipelago (Guadeloupe,  
928 French West Indies): relation with the Lesser Antilles arc system. *Bulletin de la  
929 Société Géologique de France*, 187, 3–10, doi: 10.2113/gssgfbull.187.1.3.
- 930 VILLA, I.M., RUGGIERI, G., PUXEDDU, M., & BERTINI, G. **2006**. Geochronology and  
931 isotope transport systematics in a subsurface granite from the Larderello–  
932 Travale geothermal system (Italy). *Journal of Volcanology and Geothermal  
933 Research*, 152, 20–50, doi: 10.1016/j.jvolgeores.2005.09.011.
- 934 WARR, L.N. & COX, S.C. **2016**. Correlating illite (Kübler) and chlorite (Árkai)  
935 “crystallinity” indices with metamorphic mineral zones of the South Island, New  
936 Zealand. *Applied Clay Science*, 134, 164–174, doi: 10.1016/j.clay.2016.06.024.
- 937 WHITE, N.C. & HEDENQUIST, J.W. **1990**. Epithermal environments and styles of  
938 mineralization: Variations and their causes, and guidelines for exploration.  
939 *Journal of Geochemical Exploration*, 36, 445–474, doi: 10.1016/0375-  
940 6742(90)90063-G.
- 941 WIEWIÓRA, A. & WEISS, Z. **1990**. Crystallochemical classifications of phyllosilicates  
942 based on the unified system of projection of chemical composition: II. The  
943 chlorite group. *Clay Minerals*, 25, 83–92, doi: 10.1180/claymin.1990.025.1.09.
- 944 WILSON, C.J.N., CHARLIER, B.L.A., FAGAN, C.J., SPINKS, K.D., GRAVLEY, D.M.,  
945 SIMMONS, S.F., & BROWNE, P.R.L. **2008**. U–Pb dating of zircon in hydrothermally  
946 altered rocks as a correlation tool: Application to the Mangakino geothermal field,  
947 New Zealand. *Journal of Volcanology and Geothermal Research*, 176, 191–198,  
948 doi: 10.1016/j.jvolgeores.2008.04.010.
- 949 WOJDYR, M. **2010**. Fityk : a general-purpose peak fitting program. *Journal of Applied  
950 Crystallography*, 43, 1126–1128, doi: 10.1107/S0021889810030499.
- 951 WOLDEGABRIEL, G., BROXTON, D.E., & BYERS, F.M. **1996**. Mineralogy and temporal  
952 relations of coexisting authigenic minerals in altered silicic tuffs and their utility as  
953 potential low-temperature dateable minerals. *Journal of Volcanology and  
954 Geothermal Research*, 71, 155–165, doi: 10.1016/0377-0273(95)00064-X.
- 955 ZAMI, F., QUIDELLEUR, X., RICCI, J., LEBRUN, J.-F., & SAMPER, A. **2014**. Initial sub-  
956 aerial volcanic activity along the central Lesser Antilles inner arc: New K–Ar ages  
957 from Les Saintes volcanoes. *Journal of Volcanology and Geothermal Research*,  
958 287, 12–21, doi: 10.1016/j.jvolgeores.2014.09.011.
- 959